

Lappeenranta-Lahti University of Technology LUT

School of Engineering Science

Double Degree Programme in Technical Physics

**Kramarenko Nikita**

**Medical Imaging Applicability Study of Silicon Pixel Detectors  
with PSI46dig ROC**

Examiners: D.Sc. (Tech.), Prof. Panja-Riina Luukka  
Prof. Erkki Lähderanta

Supervisor: D.Sc. (Tech.), Prof. Panja-Riina Luukka

## **ABSTRACT**

Lappeenranta- Lahti University of Technology LUT

School of Engineering Science

Double Degree Programme in Technical Physics

Kramarenko Nikita

### **Medical Imaging Applicability Study of Silicon Pixel Detectors with PSI46dig ROC**

Master's Thesis

2020

85 pages, 55 figures, 2 tables, 2 appendices

Examiners: D.Sc. (Tech.), Prof. Panja-Riina Luukka  
Prof. Erkki Lähderanta

Keywords: Medical Imaging, Silicon Pixel Detector, X-ray, Scattering, Water Phantom

The aim of the Multispectral Photon Counting for Medical Imaging and Beam Characterization (MPMIB) project is to develop a next-generation medical imaging detecting system capable of multispectral imaging. One of the ways is to employ a direct detection system based on photon counting with silicon pixel sensors, using readout electronics developed for high-energy physics experiments. This thesis contains an analysis of experiments performed at the Nuclear Safety Authority of Finland (STUK). The measuring campaign included the evaluation of thin silicon pixel detectors with X-rays and beam dosimetry in the water of a  $^{60}\text{Co}$  gamma ray source. These activities are related to the MPMIB project objectives and are supplying unique experimental data.

## ACKNOWLEDGMENTS

Being an attendant for a Double Degree Programme between the Lappeenranta-Lahti University of Technology LUT and the Electrotechnical University in Saint-Petersburg LETI made the writing of this thesis possible. I am grateful to Professor Erkki Lähderanta for the opportunity.

I would like to thank my supervisor Professor Panja-Riina Luukka for her guidance and for providing the possibility to work with highly qualified people in such an interesting field of science. Special thanks to Jennifer Ott and Erik Brücken for their priceless help and patience. I would also like to thank all of the CMS Upgrade project team for a warm welcome.

I am grateful to my parents, Roman and Larisa, for their support and love.

The work for the thesis was carried out as a part of the MPMIB project, most of the experimental data were obtained during the measuring campaign at the Nuclear Safety Authority of Finland (STUK). I would like more experiments to be carried out, but unfortunately, the raging pandemic did not allow this to happen.

Nikita Kramarenko

June 2020

# TABLE OF CONTENTS

ABBREVIATIONS .....	5
1. INTRODUCTION .....	6
2. LITERATURE REVIEW AND THEORETICAL FRAMEWORK .....	9
2.1. THE CMS EXPERIMENT .....	9
2.2. PHASE 0 .....	13
2.3. PHASE 1 .....	15
2.4. CMS DETECTORS IN MEDICAL IMAGING .....	17
2.5. IONIZING RADIATION .....	19
2.6. INTERACTION OF IONIZING RADIATION WITH MATTER.....	21
2.6.1. Interaction of electrons with matter .....	21
2.6.2. Interaction of $\alpha$ particles with matter .....	23
2.6.3. Interaction of photons with matter .....	24
2.7. SILICON-BASED IONIZING RADIATION DETECTORS .....	27
2.7.1. Properties of silicon .....	28
2.7.2. The pn-junction .....	31
2.7.3. Silicon tracking device working principle .....	34
2.7.4. Ionization energy loss in silicon detectors .....	36
2.8. RADIATION DAMAGE IN SILICON DETECTORS .....	36
2.8.1. Bulk defects.....	37
2.8.2. Surface defects .....	42
3. EXPERIMENTAL PART .....	43
3.1. THE EXPERIMENTAL SETUP .....	43
3.2. X-RAY BOX TEST .....	48
3.3. X-RAY TUBE TESTS .....	50
3.3.1. X-ray tube tests with AC-coupled silicon pixel detector G1 .....	53
3.3.2. X-ray tube tests with CMS single-chip silicon pixel detector 47A .....	55
3.4. $^{60}\text{Co}$ TEST WITH THE WATER PHANTOM.....	64
4. ANALYSIS OF RESULTS .....	74
5. CONCLUSIONS .....	75
SUMMARY .....	77
REFERENCES.....	78
APPENDICES .....	82
APPENDIX A. TEST JOURNAL.....	82
APPENDIX B. X-RAY CHARACTERISTICS.....	85

## ABBREVIATIONS

CERN	Conseil Européen pour la Recherche Nucléaire
LHC	Large Hadron Collider
SM	Standard Model
ATLAS	A Toroidal LHC Apparatus
CMS	Compact Muon Solenoid
ALICE	A Large Ion Collider Experiment
LHCb	The Large Hadron Collider Beauty Experiment
LS2	Long-Shutdown 2
ITS	Inner Tracking System
MAPS	Monolithic Active Pixel Sensor
TPC	Time Projection Chamber
NSW	New Small Wheels
SCR	Space Charge Region
AC	Alternating Current
DC	Direct Current
ROC	Readout Chip
STUK	Nuclear Safety Authority of Finland
NIEL	Non-Ionizing Energy Loss
CCE	Charge Collection Efficiency
SCSI	Space Charge Sign Inversion
ADC	Analog-to-Digital Converter
DAC	Digital-to-Analog Converter
RH	Relative Humidity

## 1. INTRODUCTION

In the year 2020 high energy physics research is essential to understand the properties of particles and their behavior. Even though many answers have already been found, much more is yet to discover.

The largest center for scientific research in Europe, Conseil Européen pour la Recherche Nucléaire (CERN) or the European Organisation for Nuclear Research, provides a wide and unique range of facilities that are used for particle physics research. The most powerful is the Large Hadron Collider (LHC) (Figure 1) that has 26.7 km of circumference, almost 10 thousands of superconducting magnets, and allows to push protons with nominal energies around 6.5 teraelectronvolts (TeV) per beam (13 TeV of total collision energy). LHC allows the extraordinary precise measurements of Standard Model (SM) parameters to find deviations or to explore physics even beyond the SM.

As it is shown in Figure 1, the LHC is equipped with four fundamental experiments: A Toroidal LHC Apparatus or ATLAS [2], Compact Muon Solenoid or CMS [3], A Large Ion Collider Experiment or ALICE [4], and The Large Hadron Collider Beauty Experiment or LHCb [5].

ALICE allows studying heavy ion physics and will be equipped with a new high-resolution silicon tracker, an upgraded muon forward tracker, and new readout chips and much more during the long-shutdown two (LS2). A new inner tracking system (ITS) of ALICE based on a CMOS monolithic active pixel sensor (MAPS) will be installed, thus allowing to host both the readout circuit and the sensor for charge collection in the same piece of silicon. The new chip is called ALPIDE and contains 1024 columns and 512 rows of pixels. New ITS has 7 cylindrical layers of ALPIDE chips which results in 10 m<sup>2</sup> total area of pixels. The extension of ITS capabilities along with a new muon detector and time projection chamber (TPC) will significantly improve the performance of ALICE.

The unique experiment among the LHC experiments studying the beauty quarks is the asymmetrically built LHCb. It will be almost entirely rebuilt during LS2. The current system based on silicon microstrip modules will be replaced with new 26 tracking layers of pixels that will receive the “heaviest irradiation of all LHC detectors“. It is extremely important to enhance the performance and radiation hardness of pixel detectors that will be operated under up to five times the instantaneous luminosity seen at Run 2.

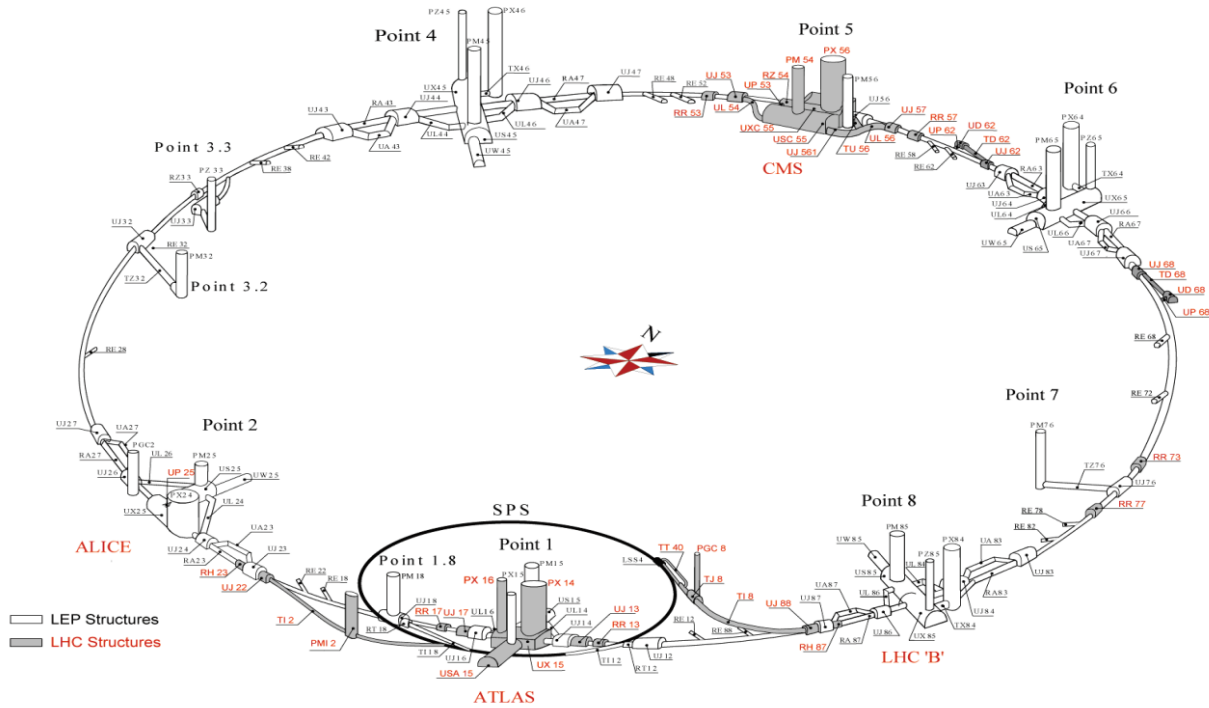


Figure 1. Overview of LHC ring and infrastructure [1]

CMS and ATLAS are general-purpose detector complexes. ATLAS has the same scientific goals as the CMS experiment which is discussed in detail in Chapter 2. The difference between them is the technical solutions and the design of the magnet system. During the LS2 ATLAS will receive new components for the electromagnetic calorimeter, thus improving the ability to preserve photons and electrons. Upgraded trigger and data-acquisition systems, as well as new small wheel (NSW) detectors, should

meet the expected requirements based on the continuously growing luminosity of the LHC.

In all of the four main LHC experiments, silicon detectors are used for tracking the particles originating from the collision. Lately, several spin-off applications for such detectors have emerged, including medical imaging applications, which require very precise and efficient detectors. This thesis work aims to investigate the medical applicability of the CMS silicon pixel detector using various x-rays.

## 2. LITERATURE REVIEW AND THEORETICAL FRAMEWORK

### 2.1. The CMS experiment

The Compact Muon Solenoid was created to study proton-proton and ion-ion collisions at very high energies and luminosities. The luminosity indicates the performance of the accelerator to produce the required number of interactions and can be calculated using Equation 1:

$$L = \frac{\gamma f k N_p^2}{4\pi \varepsilon_n \beta^*} F, \quad (1)$$

where  $f$  is frequency,  $\gamma$  is the Lorentz factor,  $k$  is the number of bunches per proton beam (around 2800),  $N_p$  is the number of protons per bunch ( $1.2 \cdot 10^{-11}$  at the start),  $\varepsilon_n$  is the normalized transverse emittance,  $\beta^*$  is the beta function at the point of interaction and  $F$  is the reduction factor [6].

The designed luminosity value of the LHC is  $L = 10^{-34} \text{ cm}^{-2}\text{s}^{-1}$  to generate 1 billion interactions. Thus, the CMS experiment had to meet the following experimental requirements:

- Efficient pattern recognition
- High reconstruction efficiency
- Fast response time to resolve bunch crossings
- High granularity to resolve tracks
- High electromagnetic energy resolution
- Good muon identification and momentum resolution for a wide range of energies

All those requirements dictate the specific detector design, which ideally would have the spherical shape, but that is not technically possible. The detector must be close to the interact region, therefore the cylindrical shape was chosen to meet the geometrical

coverage requirement and include the magnetic solenoid for the momentum measurements. The resulting detector design is shown in Figure 2.

The CMS experiment layout includes several sub-detectors as layers from the inner to the outer: the inner tracker that includes silicon strip and pixel detectors, the electromagnetic calorimeter, the hadron calorimeter, the muon system. The transverse slice of the given structure is shown in Figure 3.

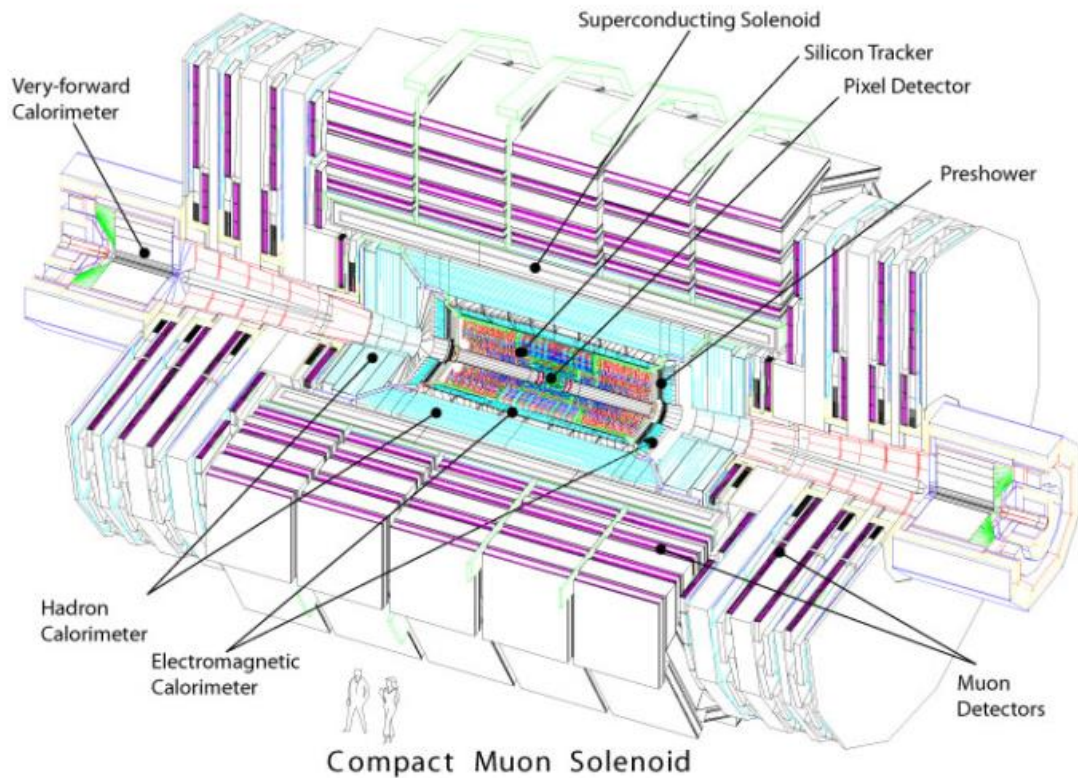


Figure 2. The CMS experiment layout [7]

The most relevant part for this work is the inner tracking system that consists of several layers of very precise silicon detectors. The system is designed according to the expected flux of charged particles. The inner tracking being the innermost part is exposed to high radiation doses, which will cause radiation damage to the silicon material. The interaction of radiation with matter will be discussed later in Chapters 2.5, 2.6. The

expected radiation doses with relation to the distance as  $\frac{1}{r^2}$  for different radii are shown in Table 1.

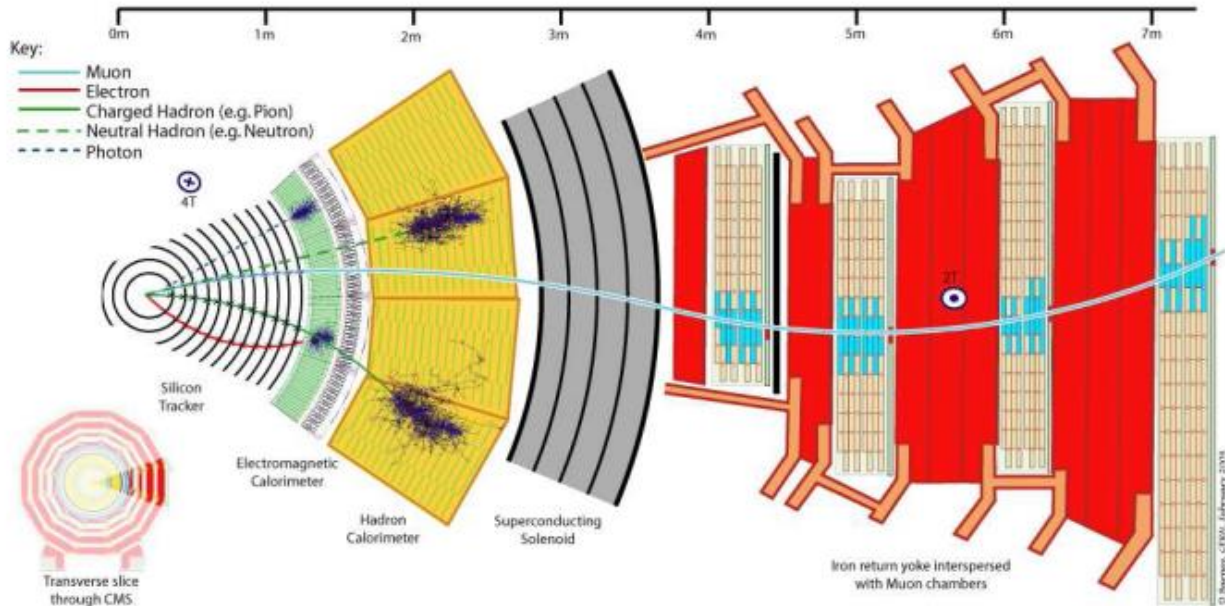


Figure 3. Transverse slice of CMS experiment [7]

As shown, the detectors are exposed to the large radiation dose, therefore this environment sets a strict requirement for the radiation hardness, which alongside granularity, and speed requirements are the greatest challenges for the silicon-based devices used in the LHC experiments- The layout of the inner tracking system is shown in Figure 4.

Table 1. Expected radiation dose and hadron fluence in radial layers of the CMS tracker for an integrated luminosity of  $500 \text{ fb}^{-1}$ , corresponding to the first 10 years of running [8]

Radius (cm)	Fast hadron fluence ( $10^{14} \text{ cm}^{-2}$ )	Dose (kGy)	Charged particle flux ( $\text{cm}^{-2}\text{s}^{-1}$ )
4	32	840	$10^8$
7	12	371	
11	4.6	190	
22	1.6	70	$6 \times 10^6$
75	1.2	7	
115	0.3	1.8	$3 \times 10^5$

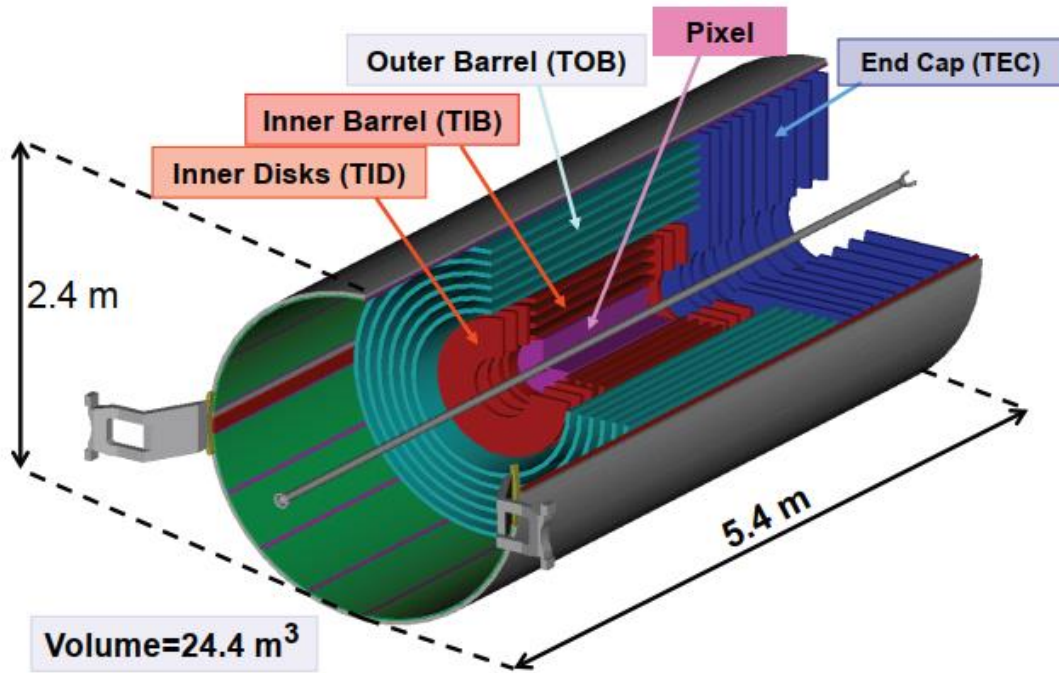


Figure 4. The CMS tracker layout overview [9]

The properties of this layout (high spatial resolution and granularity) allow reconstructing the particle tracks with high precision. The system is instrumented with approximately 206 m<sup>2</sup> of active silicon-based detectors and can detect more than 500 particles from 20 collisions per bunch crossing, the collision is happening every 25 ns [10]. Due to the radiation damage and the continuously increasing luminosity, new technical solutions have to be found and the detector upgraded to meet the physics requirements. These updates are known as phases.

## 2.2. Phase 0

The phase 0 was a detector layout which operated from 2008 until 2016. It was a complex device with a pixel detector in the center surrounded by 10 strip barrel layers with 1440 pixel and 15148 strip detector modules. It had around 66 million cells and 10 million strips that were surrounding the beam pipe. The phase 0 layout is shown in Figure 5 and Figure 6.

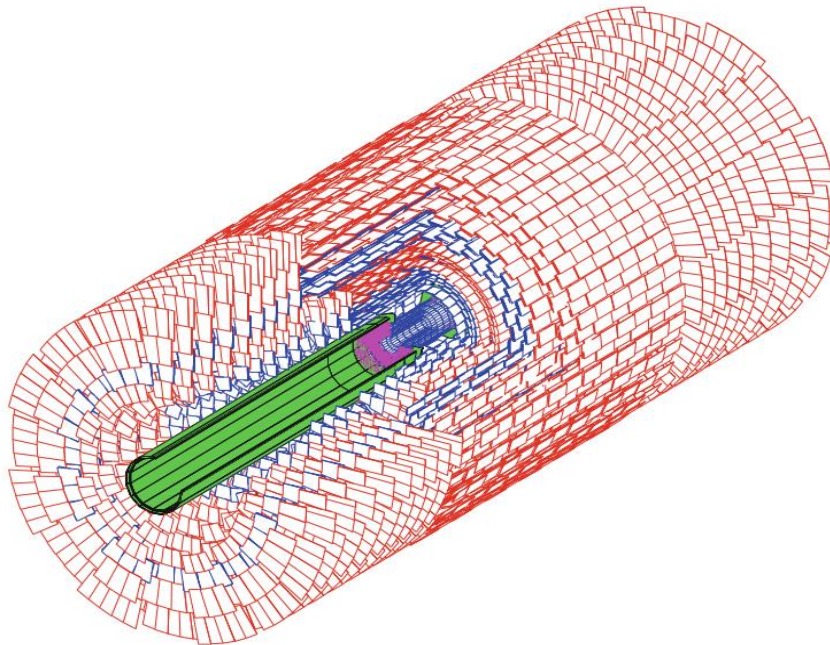


Figure 5. The CMS Phase 0 all-silicon tracker layout [10]

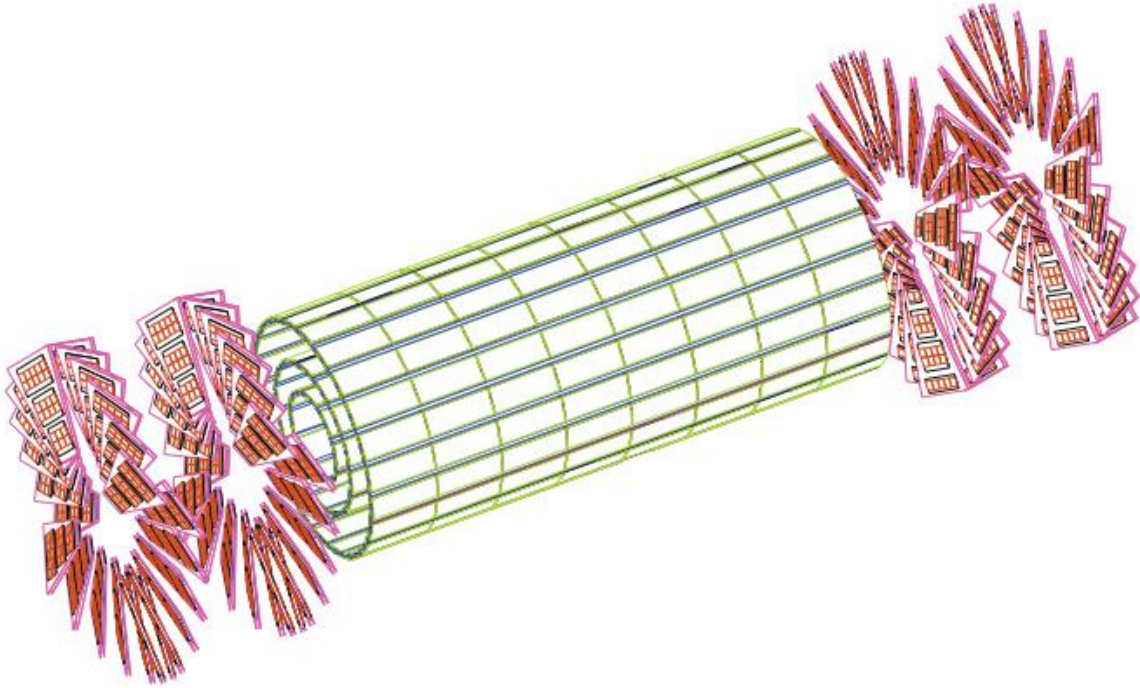


Figure 6. The CMS pixel detector layout [10]

In Figure 6 three barrel pixel layers with radii 4.4, 7.3, and 10.2 cm can be observed as well as two forward disks at each end with the turbine configuration and unique complex sensor geometry (Figure 7). Such configuration guarantees the 3D space points coverage with pseudo-rapidity up to  $|\eta| = -\ln\left(\tan\frac{\theta}{2}\right) < 2.5$ .

The pixel detector is designed in such a way that it can be replaced. As was mentioned before, the inner layers are exposed to a large radiation dose, which causes radiation damage and deteriorates their performance, thus shortening the lifetime of the detectors. At first, the plan was to replace just the innermost layer located closest to the interaction point, but the increase in luminosity achieved by LHC forced the CMS to replace the full pixel detector. The reason is simple, at higher luminosities, the phase 0 detector would have severe dead time and inefficiencies due to the limited buffers in the readout chip (ROC) and radiation damage.



Figure 7. Half of a forward disk [Courtesy of CMS/CERN/FNAL]

### 2.3. Phase 1

During the end of the year technical stop in 2017, the update named phase 1 was installed. Phase 1 has much more efficient and radiation tolerant readout chips that can perform under higher luminosities. Complete information about phase 1 can be found in [12] and [13]. Smaller beam pipe made it possible to place another layer closer to the collision point, while the radii of the second and the third layers were almost the same (3.0, 6.8, 10.9, 16 cm). One more disk was added to each endcap as well, the table with the main differences between phase 0 and phase 1 can be found in [10].

Changing the data transmission from 40 MHz analogue to 160 MHz digital solved the data throughput problem. Phase 1 has twice the number of modules in the pixel barrel while the total mass is half of the previous detector.

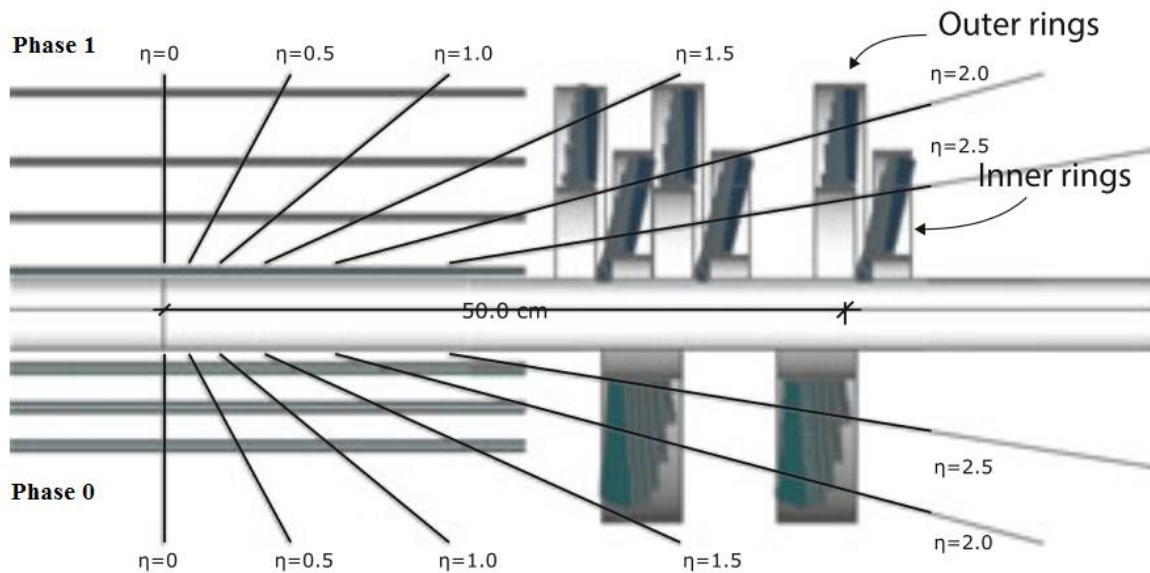


Figure 8. The layout comparison [10]

The detector used during the experimental part of this thesis is a single-chip variation of pixel modules that were built into the CMS pixel tracker during the phase 1 upgrade. The standard CMS detector has 16 ROCs and 66560 channels per pixel detector module, and in this study a version of 1 ROC was used. The CMS pixel phase 1 detector was designed to withstand the instantaneous luminosities of up to  $2 \cdot 10^{34} \text{ cm}^{-2}\text{s}^{-1}$  [33]. The single-chip variation has  $80 \times 52$  pixels with  $100 \mu\text{m} \times 150 \mu\text{m}$  size, these pixels are bump bonded to the PSI46dig readout chip. The pixels use the n+-in-n type design. The number of detector channels almost doubled compared to the original pixel detector, however, limited space was the reason to keep the number of cables running into the detector the same. The specification for the PSI46dig digital readout chip in comparison with the PSI46V2 analog one is shown in Table 2 [34].

The high spatial resolution alongside the large dynamic range can be implemented in other areas, one of which is medical imaging.

Table 2. Specifications for the PSI46V2 analog and PSI46DIG digital readout chips

Parameter	PSI46V2	PSI46dig
ROC size	7.9 mm × 9.8 mm	7.9 mm × 10.2 mm
Pixel size	100 μm × 150 μm	100 μm × 150 μm
Smallest radius	4.3 cm	2.9 cm
Settable DACs/registers	26 / 2	19 / 2
Power up conditions	not defined	default values
Pixel charge readout	analog	digitized, 8 bit
Readout speed	40 MHz	160 Mbit/s
Time stamp buffer size	12	24
Data buffer size	32	80
Output buffer FIFO	no	yes
Double column speed	20 MHz	20 MHz (40 MHz)
Metal layers	5	6
Leakage current compensation	yes	no
Data loss at max operating flux	~3.8% at 120 MHz/cm <sup>2</sup>	1.6% at 150 MHz/cm <sup>2</sup> ~3.8% at 580 MHz/cm <sup>2</sup>

## 2.4. CMS detectors in medical imaging

High energy proton or ion beams are used in medical physics for the hadron therapy to target tumors and spare healthy tissue with precision which is allowed by the deposition of intense ionization in human tissue. This technology is advantageous in case the tumor is located near critical organs when the effect of irradiation tends to be more severe. It is extremely important to have very precise and efficient equipment for such applications. It is necessary to have an accurate 3D map of the stopping power, and to create such a map for a patient, detectors originally designed for particle physics can be used. The

difference in the proton relative stopping power for different clinically relevant materials can be observed using pixel detectors.

Based on the technology originally developed for the CMS experiment, detectors for studying molecular structures were designed. This kind of pixel detector can provide excellent spatial resolution and a wide dynamic range that are required for the third- and fourth-generation light sources. Silicon can provide reasonable efficiencies for 5 keV - 30 keV photons [14], even though different materials like CdTe can be more efficient for some applications. As shown in Figure 9, the 300  $\mu\text{m}$  layer of silicon is needed to absorb photons with energies 10 keV, 1 mm for 30 keV which looks like a barrier to use it, but silicon strip detectors, which are not the object of interest of this work, can be used for tracking and for measuring the proton ranges in absorber layers behind the patient to determine the proton residual energies. This is discussed more closely in [15], [16].

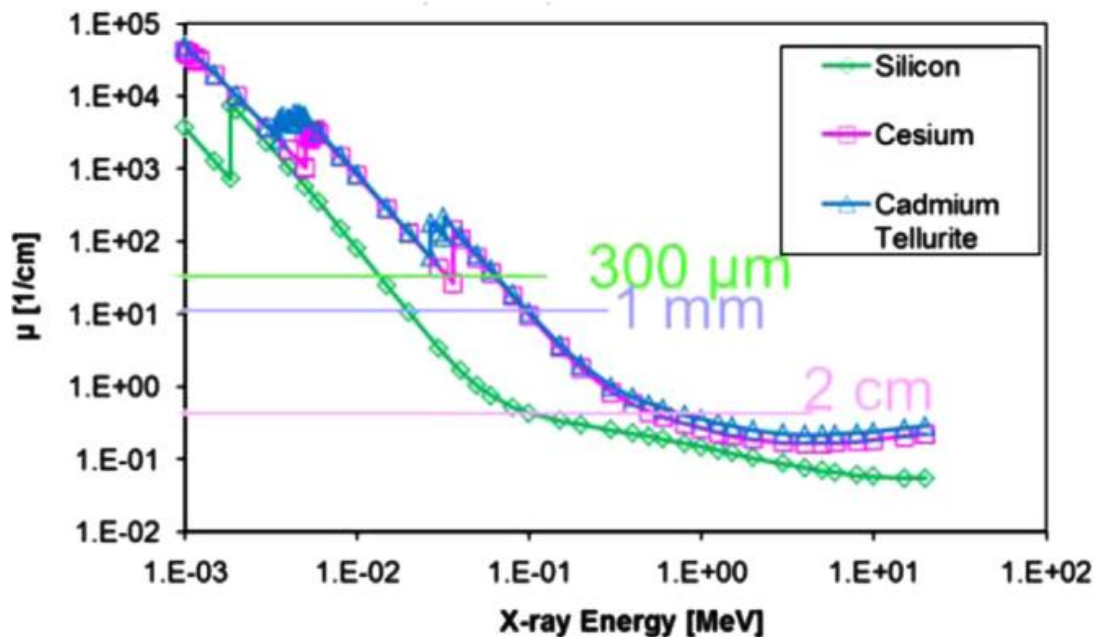


Figure 9. Photon attenuation coefficient (the reduction of the photon flux by a factor  $1/e$ ) for Silicon (300  $\mu\text{m}$ ), Cesium (2 cm), and Cadmium Tellurite (1 mm) [17]

Many recent developments are aimed to enhance the performance of tracking devices in dosimetry and imaging, including X-ray computed tomography (CT), single-positron emission CT (SPECT), positron emission tomography (PET) and time-of-flight PET (ToF-PET) [18]. The research goal is to create a low noise tracking detector with high spatial resolution and micrometer-scale granularity, that has high time resolution, is radiation hard and has a modern readout module. There is a concept of 4D detectors that holds great promises if the realization is possible, but it is important to study the applicability of already existing devices to understand the benefits and the drawbacks. In order to do that one has to understand the physics behind the processes and tracking devices.

## **2.5. Ionizing radiation**

There are different types of radiation with varying properties leading to a diverse number of effects and interactions with matter.

Sources of ionizing radiation are expected to be radioactive sources, high voltage electronic devices designed to emit X-rays and accelerators. Ionizing radiation is generated through nuclear reactions, nuclear decay, by very high temperature, or via acceleration of charged particles in electromagnetic fields. Natural sources include the sun, lightning, and supernova explosions. There are following types of ionizing radiation: alpha, beta, gamma, X-rays, and neutron radiation.

Alpha radiation occurs when atom experiences a radioactive decay, which is followed by the emission of a particle consisting of two protons and two neutrons. Alpha particles interact (excite or ionize the atom of material) and, hence, transfer energy through the electrostatic (Coulomb) forces.

Beta radiation is either an electron or a positron emitted from an atom. Lower mass, compared to alpha particles, makes it possible for beta particles to travel further distances in air and be able to penetrate thicker surfaces.

Gamma radiation is not a particle but a photon, high energy wave, which is emitted from the nucleus of an atom. Having no mass or electric charge, photons lose much less energy traveling and penetrating materials with low atomic numbers. Similar to gamma, X-rays are emitted photons, but they are emitted from an electron cloud of an atom due to the movement of an electron from a high energy level to a lower one. Interaction of X-rays and gamma rays with material causes ionization. Depending on the energy of a photon the process can flow in three different ways:

- a. A photon with low energy transfers its energy to an electron, which is, as a result of the interaction, released from the atom (photoelectric interaction).
- b. A photon with intermediate energy and electron both scatter after the interaction (Compton event).
- c. A photon with high (more than 1.022 MeV) energy disappears after the interaction and forms an electron-positron pair. The total kinetic energy of such a pair is equal to the initial photon energy. This pair is an example of directly ionizing radiation, since the result of its encounter with an electron is a destruction of the pair and creation of two gamma photons.

Neutron radiation is an emission of a neutral particle that cannot directly ionize an atom or interact with its electron cloud. Neutrons lose energy during the inelastic collision. They can ionize an atom indirectly when absorbed by making it unstable which can lead to nuclear interactions such as activation and fission. The energy released from the nucleus after the collision with neutron can be in a form of gamma ray, beta particle, or both. When a neutron is absorbed by the nucleus, energy might be released as a gamma ray, an X-ray, a beta particle, or all above together.

Ionizing or high-energy radiation devices can be split into three categories: charged particle accelerators (X-ray generators, electron accelerators, Van de Graaff accelerators), radioactive nuclide sources, and nuclear reactors.  $^{60}\text{Co}$  beam source was used during the measuring campaign at STUK, Helsinki. Its characteristics, as well as the experiments performed with CMS silicon pixel detector inside a water phantom (water phantom is a transparent box filled with water, it represents the human body, which is mostly water), are discussed in Chapter 3.

To understand the detector physics, it is necessary to know the peculiarities of different particles that can interact with matter.

## **2.6. Interaction of ionizing radiation with matter**

### **2.6.1. Interaction of electrons with matter**

There are different ways for electron - matter interaction to develop, a scheme of those interactions is shown in Figure 10.

Electron - matter interactions are classified into elastic and inelastic. In the case of elastic interaction, there is no energy transfer from electron to matter. Electrons that are coming from the incident beam pass the sample without any interaction and form the direct beam (Figure 10). If an electron is deflected from the initial direction by Coulomb interaction with the positive potential inside the electron cloud, then it loses a negligible amount of energy. In the case of inelastic interactions, the energy transfers from the electron to a matter. For heavy materials and high electron energies interaction, the vast part of energy loss is due to bremsstrahlung radiation, which is essentially a photon produced by the deceleration of a charged particle. The average energy loss can be calculated with Equation 2 [20].

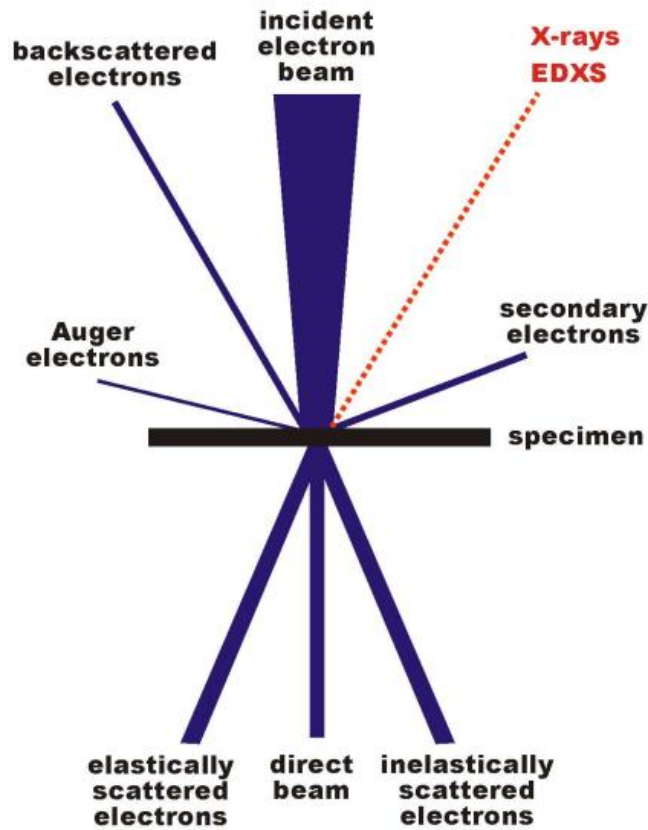


Figure 10. Scheme of electron-matter interactions arising from the impact of an electron beam onto a specimen. A signal below the specimen is only observable if the thickness is small enough to allow some electrons to pass through [19]

$$-\left(\frac{dE}{dx}\right) \approx \frac{4N_a Z^2 \alpha^3 (\hbar c)^2}{m_e^2 c^4} E \ln \frac{183}{Z^3}, \quad (2)$$

where  $\frac{dE}{dx}$  is the energy loss with distance,  $N_a$  is a number of atoms per volume,  $Z$  is the atomic number,  $\alpha$  is the fine structure constant [20].

### 2.6.2. Interaction of $\alpha$ particles with matter

There is not much difference in the electromagnetic interaction of  $\alpha$  particles and electrons of the same kinetic energy with the matter regarding scattering. However, the behavior of interaction is highly dependent on energy loss. Omitting the nuclear reactions of  $\alpha$  particles for energies less than 10 MeV we can use the terms of non-relativistic theory.

The average loss of energy over a certain path can be described by Bethe's formula (Equation 3) [20]:

$$-\left(\frac{dE}{dx}\right) \approx \frac{4\pi z^2 e^2}{mv^2} NZ \ln \frac{2mv^2}{I}, \quad (3)$$

where  $ze$  is the  $\alpha$  particle charge,  $v$  its velocity,  $N$  is the number of atoms per volume,  $I$  is the mean excitation energy of the atomic electrons [20].

For low velocities, electrons can be captured and lost due to the charge of the  $\alpha$  particle that is no longer a constant value. The mean free path for capture and loss of the electron is strongly dependent on the particle velocity. Calculations have been done by Bohr [21], Bethe [22], and others.

The ionization of  $\alpha$  particles can be described by the specific and total ionization. The specific ionization gives the number of particles per certain path length and depends on the velocity of the particle. The results of the total ionization measurement performed by Jesse and Sadauskis [23] show that the energy needed to form an ion pair is almost independent of the particle velocity.

As for the elastic scattering of the  $\alpha$  particle, for heavy atoms, the cross-section can be written using the Rutherford formula (Equation 4) [20]:

$$\frac{d\sigma}{d\Omega} \approx \frac{z^2 e^4 Z^2}{16E^2 \sin^4 \frac{\theta}{2}} NZ \ln \frac{2mv^2}{I}, \quad (4)$$

where  $E$  is the kinetic energy of the  $\alpha$  particle. Some correction factors are needed for lighter atoms. Depending on the mass relation either the first (Equation 5) or the second (Equation 6) case should be chosen.

$$\frac{(M_a \cos \theta + \sqrt{M_a^2 - M^2 \sin^2 \theta})^2}{(1 + \cos \theta)^2 M_a \sqrt{M_a^2 - M^2 \sin^2 \theta}}; \text{ if } M < M_a, \quad (5)$$

$$2 \frac{M_a^2 (1 + \cos^2 \theta) - M^2 \sin^2 \theta}{(1 + \cos \theta)^2 M_a \sqrt{M_a^2 - M^2 \sin^2 \theta}}; \text{ if } M > M_a. \quad (6)$$

For  $\alpha$  particles with energies less than 10 MeV that were taken into consideration in this chapter, multiple scattering is not viable because the number of collisions on their path is too small.

### 2.6.3. Interaction of photons with matter

Comparing all types of radiation, it is known that gamma and X-ray radiation interact with matter the most. As was previously mentioned, gamma and X-rays interact with detectors and absorbers in three ways: photoelectric interaction, Compton event, and pair production.

Photoelectric interaction or absorption causes the gamma ray to lose all of its energy after the contact with a bound atomic electron. In case a gamma ray has more energy than the amount needed to break the bound, the excess energy is transferred to the unbounded electron as kinetic energy. This process is important for gamma ray detection because the resulting pulse falls in the full-energy peak after the gamma ray loses all of its energy [24]. The probability of such interaction depends on the gamma ray energy  $E_\gamma$ , the energy required to break the bond between the electron and atom, and the atomic number of matter  $Z$ . In the predominant number of detectors, characteristic X-rays are absorbed in coincidence with photoelectron, and, therefore, the output has a dependence

of the total gamma ray energy. For gamma rays with small energies, the probability of photoelectric absorption is high.

Important note for the detector physics is that more than 80% of the interactions involve K electrons [24], which are electrons of the innermost electron shell, hence electrons with tightest bonds. In detectors active volume quickly stops the photoelectron, the emission of a pulse with an amplitude proportional to the photoelectron energy happens as a result. This photoelectric absorption is the primary interaction for gamma rays, X-rays with low energies, and bremsstrahlung. In small detectors, K X-rays can escape the active volume. Those escapes can be seen in the observed spectrum as escape peaks. This peak depends on the energy of the escaped X-ray and appears below the full-energy peak. Below the so-called K edge, the probability of interaction increases to the point of the binding energies of L electrons (Figure 11).

Mass attenuation coefficient can be written as  $\mu = \frac{N_A \sigma}{A}$ , where  $\sigma$  is a reaction cross-section ( $\text{cm}^2$ ),  $A$  is the atomic weight of the matter. Mass attenuation coefficient can be understood as the electron effective cross-sectional area per mass of the matter.

Compton scattering is an interaction of a gamma ray with either free or weakly bounded electron. There is a partial energy transfer which is determined by the conservation of energy and momentum. After the interaction electron is free and has the energy difference between energy loss of gamma ray and the electron binding energy as its kinetic energy. Depending on the amount of transferred energy, gamma ray, and electron scatter in different directions. For an electron to move in the direction of gamma ray before the interaction and for gamma ray to scatter at  $180^\circ$  to the angle of incidence energy needed is shown in Equation 7 [24] for a gamma ray and Equation 8 [24] for an electron.

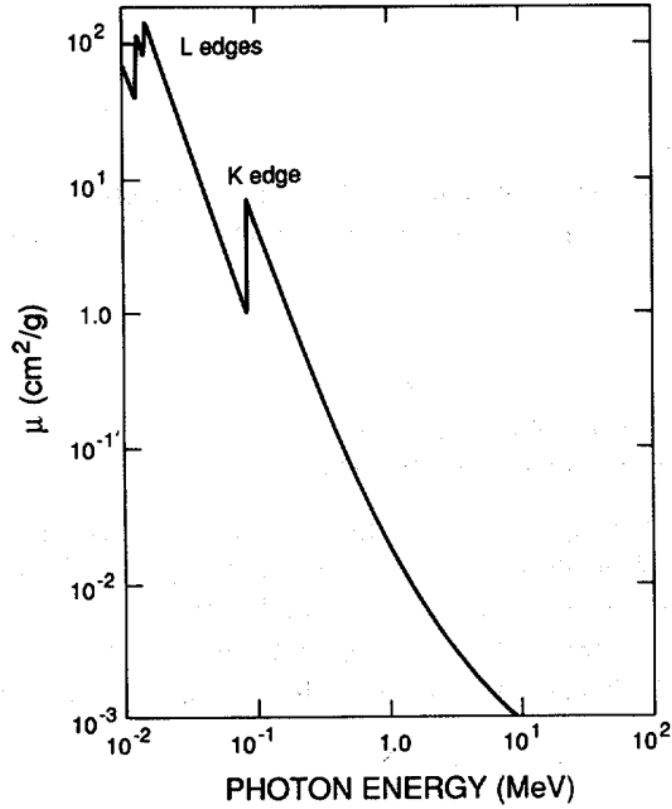


Figure 11. Photoelectric mass attenuation coefficient of lead [24]

$$E'_\gamma(\min) = \frac{m_0c^2}{\left(\frac{2 + m_0c^2}{E}\right)} = \frac{m_0c^2}{2} = 256 \text{ keV}; \text{ if } E \gg \frac{m_0c^2}{2}, \quad (7)$$

$$E_e(\max) = \frac{E}{\left(\frac{1 + m_0c^2}{2E}\right)} = \frac{E - m_0c^2}{2} = E - 256 \text{ keV}; \text{ if } E \gg \frac{m_0c^2}{2}, \quad (8)$$

where  $E'_\gamma$  is a scattered gamma ray energy,  $E_e$  is scattered electron energy,  $m_0c^2$  is the rest energy of an electron, which is equal to 511 keV. Characteristics gamma photons have the same energy after the positron-electron annihilation at the thermal energy.

If the angle of scattering is  $\varphi \simeq 0^\circ$  the energies of scattered and incident gamma rays are almost equal since the scattered electron takes almost no energy from the interaction (from almost zero to the energy given in Equation 7). The probability of

gamma ray to interact with the nucleus hardly depends on an atomic number, but certainly depends on the electron density.

For high energy gamma rays (at least 1.022 MeV) pair production is possible. Electron-positron pairs can be created under the influence of the electromagnetic field close to the nucleus. For gamma rays with energy more than a pair production threshold, all excess energy becomes kinetic energy shared between the electron and the positron. After the pair production process slows down in the matter, positron and electron combine and annihilate each other releasing two gamma rays with energies of 0.511 MeV. Those low energy gamma rays may either interact with the matter or escape it.

There are three ways for those two gamma rays to act inside a detector:

- a. Both gamma rays are absorbed and the full energy peak in the measured spectrum is observed.
- b. One of the gamma rays escaped the matter, then a single-escape peak is observed. This peak is located 0.511 MeV below the full energy one.
- c. If both gamma rays escaped the detector medium, then a double escape energy peak located 1.022 MeV below the full energy one is observed.

Naturally, the height of those three peaks depends on the incident gamma ray energy.

## **2.7. Silicon-based ionizing radiation detectors**

Silicon-based detectors are undeniably important and widely used in high energy physics. This chapter reviews some basic properties of silicon that made it the leading semiconductor element, the pn-junction formation, and the operation principle of silicon detectors. Also, some articles related to the radiation damage mechanisms and leakage current issues are reviewed.

### 2.7.1. Properties of silicon

Silicon has asserted dominance as the leading semiconductor element used for position-sensitive detectors. This material can be used at room temperature since the band gap is about 1.12 eV which is much more than the thermal energy at normal room temperature. Silicon is a group IV element; therefore, it has four electrons on the outer energy level that can form chemical bonding. The covalent bonds formed with adjacent silicon atoms explain the electric conductivity and, therefore, resistivity which is an essential parameter for detectors (the importance of resistivity for detector physics will be discussed later in this chapter). Bound electrons can be excited by different energy sources including light, temperature, gamma rays, and X-rays. The main reason for the wide usage of silicon as detector material is the very good intrinsic energy resolution of Si: It produces one electron-hole pair for every 3.6 eV particle crossing the medium releases [10]. The amount of released energy depends on the material. On average, an ionizing particle loses 390 eV/ $\mu\text{m}$  in silicon and creates 108 electron-hole pairs per  $\mu\text{m}$ , which is high and can be explained by the high silicon density.

For intrinsic silicon, in the absence of impurities, there are  $1.45 \cdot 10^{10}$  free charge carriers in one cubic centimeter at 300 K and the valence band is full, while the conduction band is empty. The concentration of electrons and holes are equal,  $n_i = n = p$ . To change the conductivity some additional states in the forbidden region have to be added. To do it impurities either donors or acceptors are added, the process of adding impurities to increase the probability to excite charged particles according to the Fermi-Dirac distribution function is called doping.

Dopant concentration defines the concentration of majority charge carriers. The densities of charge carriers can be written using the following Equation 9 and Equation 10 [10]:

$$n = N_C e^{-\frac{E_C - E_F}{k_B T}} \text{ with } N_C = 2 \left( \frac{2\pi m_e^* k_B T}{h^2} \right)^{\frac{3}{2}}, \quad (9)$$

$$p = N_V e^{-\frac{E_F - E_V}{k_B T}} \text{ with } N_V = 2 \left( \frac{2\pi m_h^* k_B T}{h^2} \right)^{\frac{3}{2}}, \quad (10)$$

where  $N_C$  and  $N_V$  are effective state densities for conduction and valence bands respectively.  $E_C$ ,  $E_V$ ,  $E_F$  stand for energies for the conduction band, valence band, and Fermi level.  $m_e^*$  and  $m_h^*$  are the effective masses of electrons and holes.

An important equation is the mass action law that is used both for intrinsic and doped material (Equation 11) [10]:

$$n \cdot p = n_i^2 = N_C \cdot N_V e^{-\frac{E_g}{k_B T}}, \quad (11)$$

where  $E_g = E_C - E_V$  is a band gap energy.

To understand the mechanism behind conductivity and resistivity, it is important to know about drift velocity  $v_D = \mu E$  and charge carrier mobility  $\mu$ . Mobility is the ability of a charge carrier to move and, microscopically, can be defined with the time passed between two scattering processes  $\tau_s$  (Equation 12) [10]:

$$\mu_{e,h} = \frac{e\tau_s}{m_{e,h}^*}. \quad (12)$$

Then the conductivity and its inverse, resistivity, can be written as Equation 13 and Equation 14 [10]:

$$\sigma = e(\mu_e n + \mu_h p) \left[ \frac{1}{\Omega m} = \frac{S}{m} \right], \quad (13)$$

$$\rho = \frac{1}{\sigma} = \frac{1}{e(\mu_e n + \mu_h p)} [\Omega m]. \quad (14)$$

For a doped material, with one dominant type of impurity, the base resistivity can be written as Equation 15 [10] and the density of the impurity of either type is higher than the concentration of intrinsic carriers.

$$\rho = \frac{1}{e(\mu N_{D/A})}. \quad (15)$$

The base resistivity parameter is extremely important for detectors since it is inversely proportional to its minimum operational voltage [10].

To understand the process inside a real device with a dynamic equilibrium one can analyze Figure 12 [10], which shows the continuous recombination of electron-hole pairs. Only in the existence of photon exchange and fulfilling the energy and momentum conservation laws, the recombination is possible.

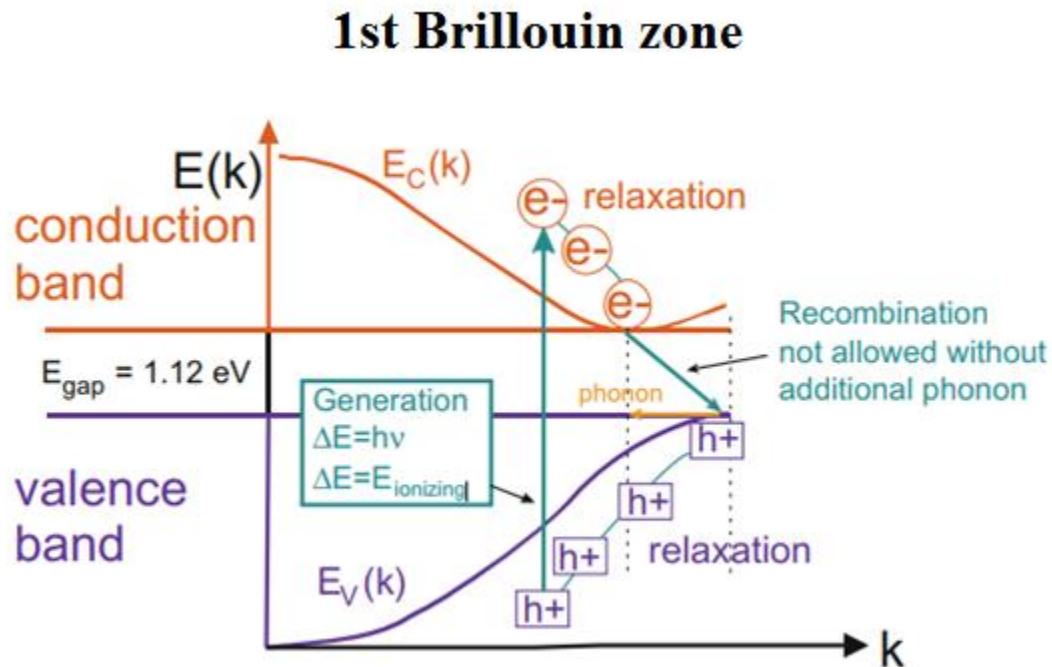


Figure 12. Electron-hole pair generation by a photon in silicon [10]

In the real device, second-ordered effects define the recombination rate. Not only those additional energy levels act like traps, but, according to the Schokley-Read-Hall theory, they (deep levels) act like generation centers for electron-hole pairs. Those

mechanisms bring a huge impact on the lifetime of the charge carriers and hence on the device characteristics like intrinsic leakage current.

### 2.7.2. The pn-junction

In an intrinsic semiconductor, the number of electrons generated by an ionizing particle is by several orders of magnitude lower than the number of free charge carriers, so it is impossible to distinguish the signal-generated charge carriers from the free charge carriers. Therefore, one needs to reduce the number of free charge carriers within the detector volume. It can be achieved either through cooling, which is not practical, or through the depletion of the semiconductor.

To deplete the semiconductor or to create the space charge region (SCR) there has to be a reverse-biased pn-junction. In this configuration p- and n-type semiconductors are merged. The majority charge carriers move into the opposite region to reach equilibrium. Only ionized dopant atoms are left behind, and they form the built-in electric field. This movement can be described by Fick's first law (Equation 16) [10]:

$$j_{diff} = -eD\nabla n, \quad (16)$$

where  $D$  is a diffusion constant and  $\nabla n$  is a concentration gradient. The principle of an SCR creation is shown in Figure 13 [10].

The space charge region or depletion region has very high resistivity due to the lack of charge carriers in it. The resistance of this region can be controlled with an external electric field. When the directions of the built-in field and the external field coincide, the width of the depletion region increases, and vice versa. Total depletion width can be written as a function of built-in potential (Equation 17) [8]:

$$w = \left[ \frac{2\varepsilon_{Si}}{q} \left( \frac{N_A + N_D}{N_A N_D} \right) V_{bi} \right]^{\frac{1}{2}}, \quad (17)$$

where  $\varepsilon_{Si}$  is the permittivity,  $V_{bi}$  is the built-in potential.

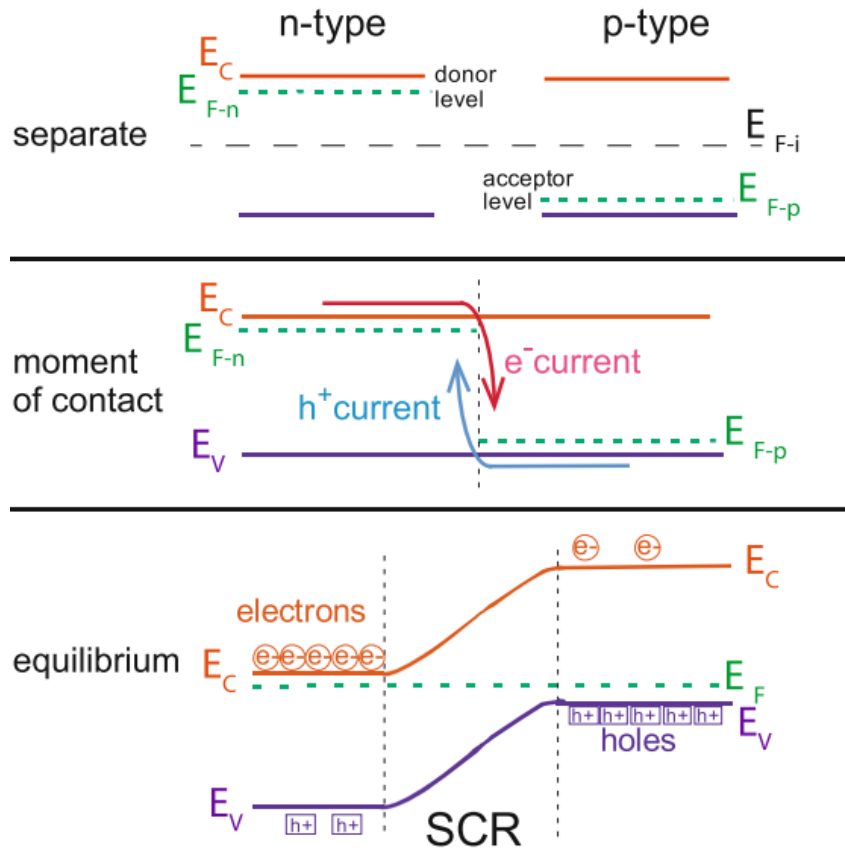


Figure 13. Behavior of a pn-junction, SCR formation [10]

Depending on the applied voltage the pn-junction can be either forward- or reverse-biased. When the negative voltage is applied to the n-type region and the positive to the p-type, the current can flow (forward-bias), when the positive voltage is applied to the n-type region and the negative to the p-type, the resistance of the junction increases and the current flow reduces (reverse-bias). Larger depletion width suitable for the detector applications can be realized by applying reverse-bias voltage. Depending on the concentrations  $N_A$  and  $N_D$  the depletion width can be larger on one side. So for the case where  $N_D \gg N_A$ , the depletion width on the p-side ( $x_p$ ) is larger than the width on the n-side ( $x_n$ ). Hence  $w$  from Equation 18 becomes Equation 19 [8]:

$$w \cong x_p = \left[ \frac{2\epsilon_{Si}(V_{bi} \pm V_{bias})}{qN_{eff}} \right]^{\frac{1}{2}}, \text{ with } N_{eff} = |N_D - N_A|. \quad (18)$$

When the full depletion voltage (Equation 19) [8] is applied, the maximum depletion width is reached:

$$V_{FD} = \frac{qN_{eff}d^2}{2\epsilon_{Si}}, \quad (19)$$

where  $d$  is the junction thickness. The full depletion voltage is a very important parameter for detector operations. One has to operate the sensor with a minimum possible voltage value to reduce the power consumption and to keep it below the level of breakdown. Usually, there is a safety factor of at least 2 between the operational (depletion) voltage and the breakdown voltage.

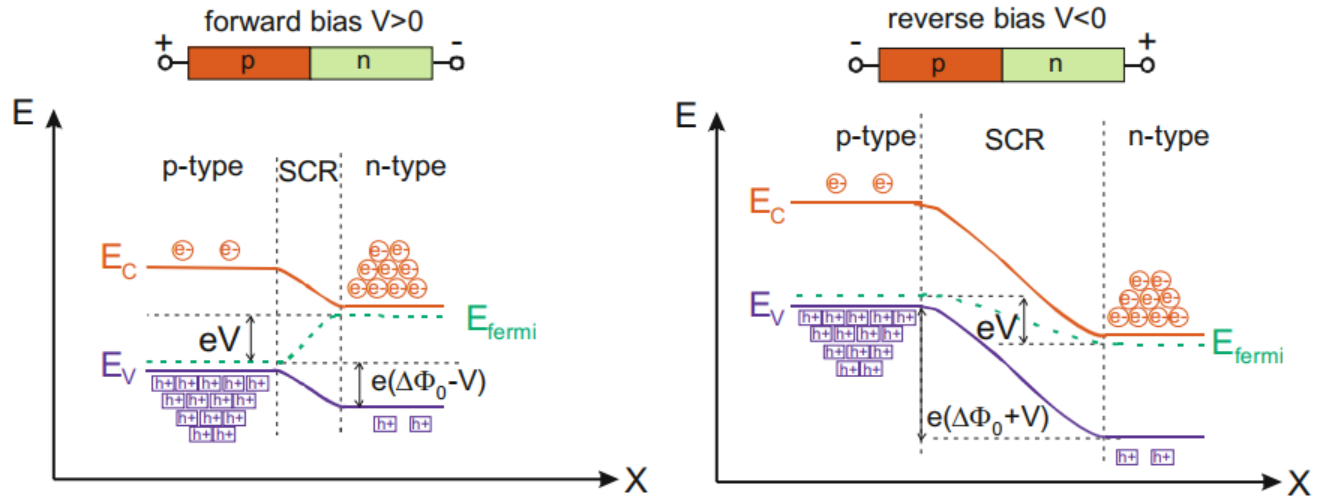


Figure 14. Forward and reverse bias cases [10]

When the forward bias is applied, the barrier decreases and the major charge carriers are allowed to move through the diode. In the case of the reverse bias, the width of the depletion region and the barrier increases.

In a situation when the bias voltage is larger than the full depletion voltage, a new electric field forces the electron-hole pairs to leave the SCR, the Schottky-Read-Hall

emissions now dominate the emission process. This is a reason for higher values of the leakage current which is, of course, an undesired effect. In fact, the leakage current increases significantly only when a breakdown occurs. In the normal operating range the leakage current is quite stable (seen as saturation in the IV curve after the depletion). The leakage current can be described by Equation 20 [10]:

$$I_L = \frac{1}{2} e \frac{n_i}{\tau_L} w \cdot A, \quad (20)$$

where  $A$  is a surface of the junction and  $\tau_L$  is the effective lifetime completely defined by the impurities.

### 2.7.3. Silicon tracking device working principle

To create a particle detector one has to understand the requirements to a certain structure and has to consider global parameters, including total leakage current and full depletion voltage, which define the performance of the device. Addressing the structure requirements, the reverse-biased pn-junction with a fully depleted space charge region has to be exposed to the radiation in order to detect a particle. When an ionizing particle penetrates the detector volume, it generates electron-hole pairs on its path (Figure 15 on the right). In the electric field, holes drift to the  $p^+$  doped areas while electrons drift to the  $n^{++}$  areas, a fast current pulse flows to the electronic readout (shown in Figure 15 on the left). Depending on the structure of the detector it can register either holes or electrons as a signal. The electrode geometry defines what charge carriers are being registered. For the standard CMS pixel detector with the n-in-n structure, where the detector bulk is n-doped, and also the pixels are n-doped, electrons are being registered. The n-in-n structure has faster charge collection and a lower charge collection efficiency (CCE) degradation as benefits, compared to the p-in-n structure. If the detector is p-type pixels on n-type bulk the holes are registered.

Electrodes can be segmented in different ways: pixels, strips, and pads. The idea of dividing the sensor into small cells allows the individual readout of each cell. The interconnections are made with bump bonds, usually from PbSn, In, etc.

Under the full depletion voltage, the SCR extends through the entire semiconductor bulk and the detector can be compared to a simple capacitor, where the semiconductor media is sandwiched between two electrodes. The capacitance is determined as Equation (21):

$$C = \frac{A \cdot \epsilon_0 \cdot \epsilon_{Si}}{d}; C_{bulk} = \frac{\epsilon_0 \cdot \epsilon_{Si}}{w} = \sqrt{\frac{\epsilon_0 \cdot \epsilon_{Si}}{2\mu\rho V_{bias}}}, \quad (21)$$

where  $A$  is area and  $d$  is a distance between electrodes,  $\epsilon_{Si}$  is the permeability.

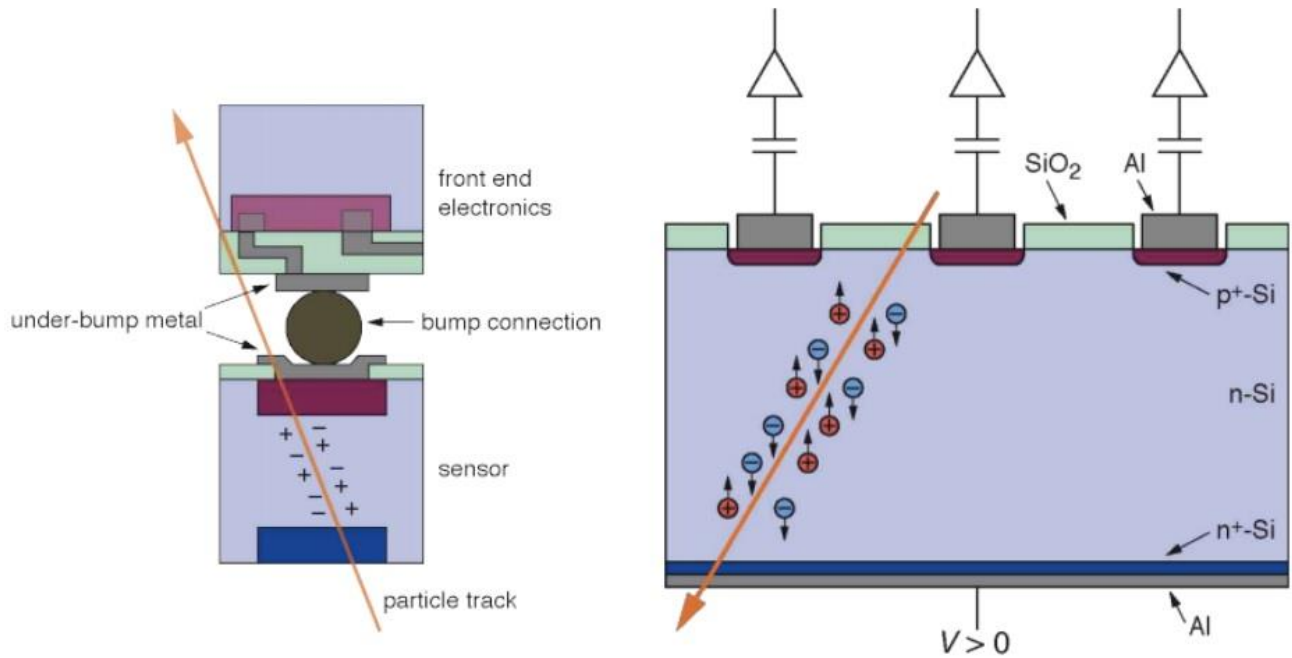


Figure 15. A schematic cross-section of the silicon detector [39]

The readout can be arranged in a form of capacitive coupling (AC-coupling) (shown in Figure 15). AC-coupling is used to transfer separated AC signals while the DC component of an incident current is blocked by a capacitor. The DC can charge the

capacitor, but cannot pass through. The impedance of the capacitor determines the current amplitude and voltage of a transferred AC signal. This readout arrangement was used for the CMS AC-coupled silicon pixel detectors used in the experimental part of the thesis.

#### 2.7.4. Ionization energy loss in silicon detectors

The particle that penetrates the semiconductor bulk interacts with matter mostly through two processes: the elastic scattering on the matter's nucleus, and the electromagnetic interaction. By the electromagnetic interaction, one can understand the inelastic collisions with electrons of the semiconductor atoms. Electrons absorb the energy and transit to the conduction band, leaving holes in the valence band. Excited electrons in the conduction band behave as free carriers. A more complete description of the mean energy loss compared to Equation 3 can be given by the Bethe-Bloch formula (Equation 22) [8]:

$$-\left(\frac{dE}{dx}\right) = 2\pi N_A r_e^2 m_e c^2 \rho \frac{Z}{A} \frac{q^2}{\beta^2} \left[ \ln \left( \frac{2m_e c^2 \beta^2 \gamma^2 E_{kinetic}^{max}}{I} \right) - 2\beta^2 - \delta \right], \quad (22)$$

where  $r_e$  is the classical electron radius,  $q$  is the charge of the incident particle,  $Z, A$  - atomic number and atomic weight of the matter,  $\rho$  is its mass density,  $I$  is the mean excitation energy of the matter,  $E_{kinetic}^{max}$  is the maximum energy transferred during the single collision,  $\beta$  is a  $\frac{v}{c}$  of the incident particle,  $\gamma = (1 - \beta^2)^{-\frac{1}{2}}$ ,  $\delta \approx \ln(\gamma) + \zeta$  is density correction, where  $\zeta$  is a material constant [8].

#### 2.8. Radiation damage in silicon detectors

Described in paragraphs 2.6.1 - 2.6.3, 2.7.4 interactions of radiation with matter can cause damage to a semiconductor device, especially in the intense radiation environment that is needed for high energy physics studies. The radiation damage is an

important limiting factor that has to be taken into consideration whenever a detector is designed. There are two types of defects caused by radiation: the bulk and the surface damage. The following sections contain brief information about both.

### **2.8.1. Bulk defects**

The penetration of matter by an energetic particle coexists with energy losses during ionizing and non-ionizing processes. These processes are the reason for both electron-pair generation (ionizing) and lattice atom displacements (non-ionizing). When the atom is missing from its normal lattice position, the defect is called vacancy. Due to the collision, the atom can leave its place in a crystalline lattice and move forward to create a vacancy and an interstitial defect which combined form a Frenkel pair. Naturally, the high enough intense energy radiation creates a lot of Frenkel pairs that form defect complexes or clusters (Figure 16) and alter the electrical and optical properties of the device.

Some vacancies and interstitials recombine and leave no damage [25], but some diffuse from the damaged region and interact with other defects forming complexes or react with impurities (carbon, oxygen, etc.) that are common for silicon.

There is a significant difference between the type of damage dealt by light (photons, low-energy electrons) and heavy (protons, neutrons) particles. The dependence of damage on the type and the energy of particle for non-ionizing energy loss (NIEL) has been observed in [26]. As mentioned in [27], the bulk damage for gamma radiation of  $^{60}\text{Co}$  photons (1.17 MeV and 1.33 MeV) is mostly a result of Compton electrons interactions with atoms. Electrons scattered from  $^{60}\text{Co}$  photons have energies about a few hundred keV [28], which is, according to [29], enough to move one or two silicon atoms from their position in a crystal lattice. Regardless of the particle type or its energy, the transferred energy between the collisions defines the damage [10].

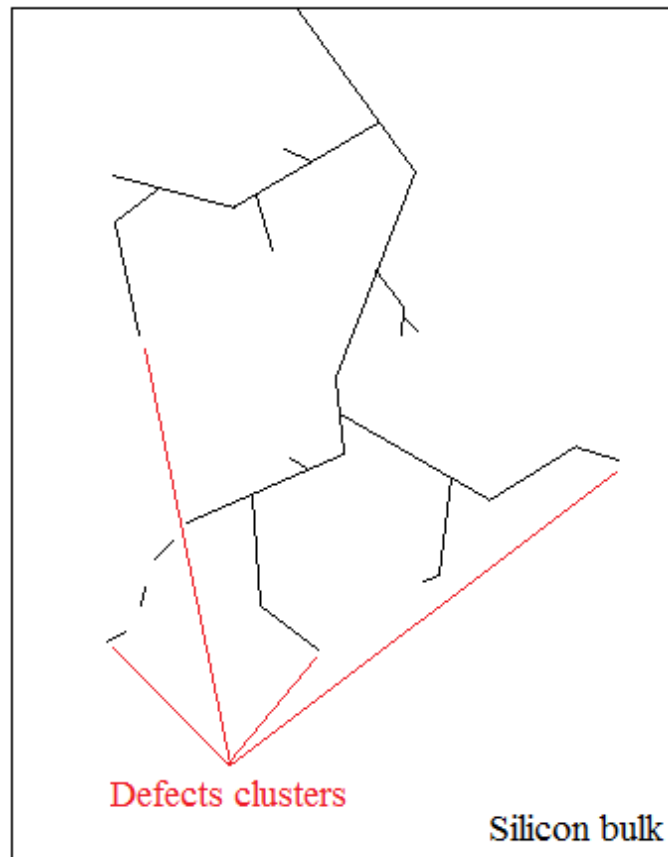


Figure 16. Schematic illustration of damage dealt by incident radiation (deep level cluster defects) in a silicon bulk

For different defect level locations, there are corresponding effects. Shown in Figure 17 [10], different level defects have their effect on the macroscopical detector performance.

All the defects are located in the bandgap. Figure 17: (a) are mid-gap levels which are responsible for the generation of dark current and decreasing the lifetime of charge carriers inside the material; (b) are donor and acceptor levels that contribute to the effective space charge and the charge defects creation; (c) are deep levels with traps for electrons and holes, that lower the (CCE) and decrease the signal; (d) the inter-center charge transfer model, according to which, defect clusters enhance the effects [10].

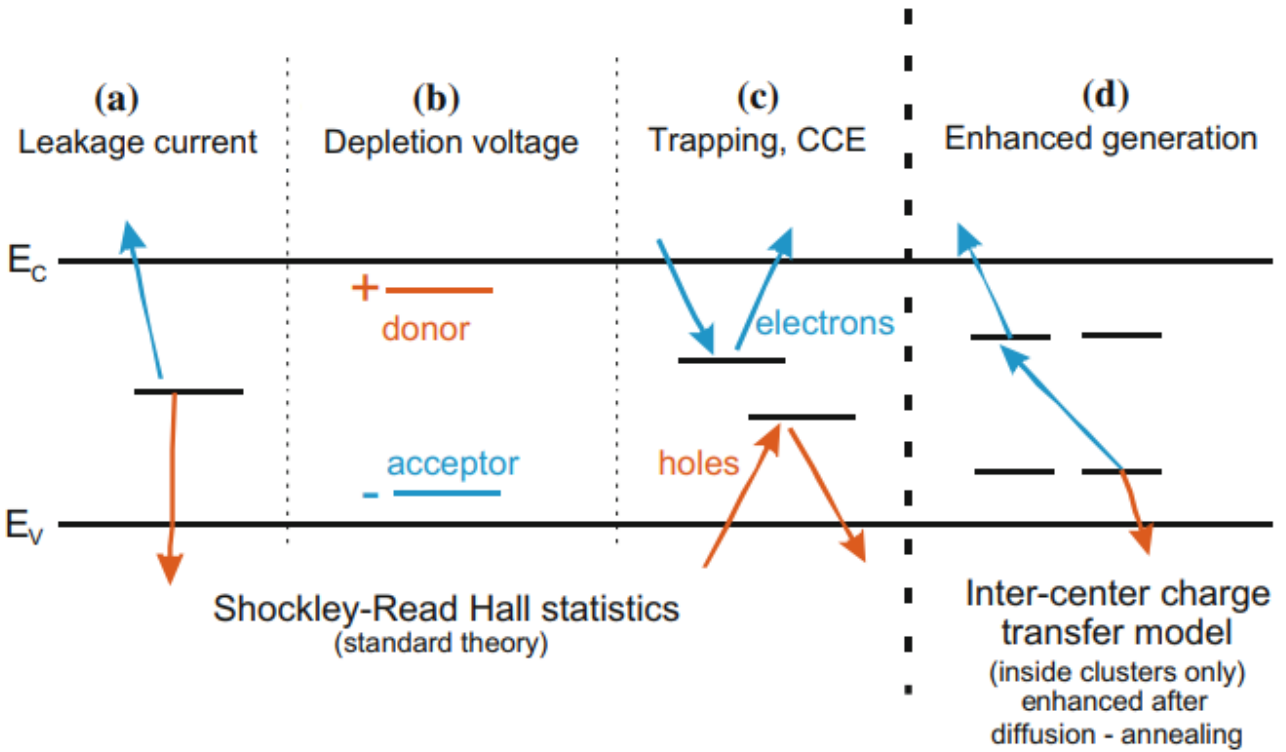


Figure 17. Locations of radiation-induced defects in the silicon bandgap and their effects [10]

Properties of silicon devices are affected when defects are present in the device bulk. Some of these properties are described below:

- 1) Leakage current is mostly affected by deep level, cluster defects that act as generation/recombination centers. The leakage current increases linearly with the fluence  $\Phi$  (an accumulated particle flux) (Equation 23) [30]:

$$I_{vol} = \frac{\Delta I}{V} = \alpha \cdot \Phi, \quad (23)$$

where  $V$  is the volume of the silicon bulk,  $\alpha$  is the leakage current rate, according to the RD48 collaboration report, the leakage current rate can be derived as Equation 24 [31]:

$$\alpha = (3.99 \pm 0.03) \times 10^{-17} \frac{A}{cm}. \quad (24)$$

After 80 minutes of annealing at 60 °C. Annealing is damage reordering under the temperature over time, it helps to reduce the damage caused by defects.

The leakage current strongly depends on the operating temperature, the dependence can be written as Equation 25 [8]:

$$I(T) \propto T^2 \exp\left(-\frac{E_g}{2k_B T}\right), \quad (2.25)$$

where T is the operating temperature,  $E_g$  is the bandgap.

- 2) Depletion voltage. Under accumulating radiation, the n-type detector bulk is compensated to the point that the effective doping concentration becomes zero and then goes through sign inversion to become effectively p-type. This is caused by the radiation-induced deep level defects. This phenomenon is referred to as the Space Charge Sign Inversion (SCSI). At first, the increase in fluence decreases the full depletion voltage because the donors are being removed. Further fluence increase causes negative space charge domination and type inversion (Figure 18) [10].
- 3) Charge trapping is induced by radiation as more trapping centers are created within the depletion region. In the absence of charge carriers, trap centers are empty and signal charges can be trapped. That leads to the reduction of the signal amplitude. The effective trapping time can be written as Equation 26 [10]:

$$\tau_{eff} = \frac{1}{N_i(1 - P_i)\sigma_i v_t}, \quad (26)$$

where  $N_i$  is the concentration of trapping centers,  $P_i$  is the occupation probability,  $\sigma_i$  is the charge carrier cross-section,  $v_t$  is thermal velocity.

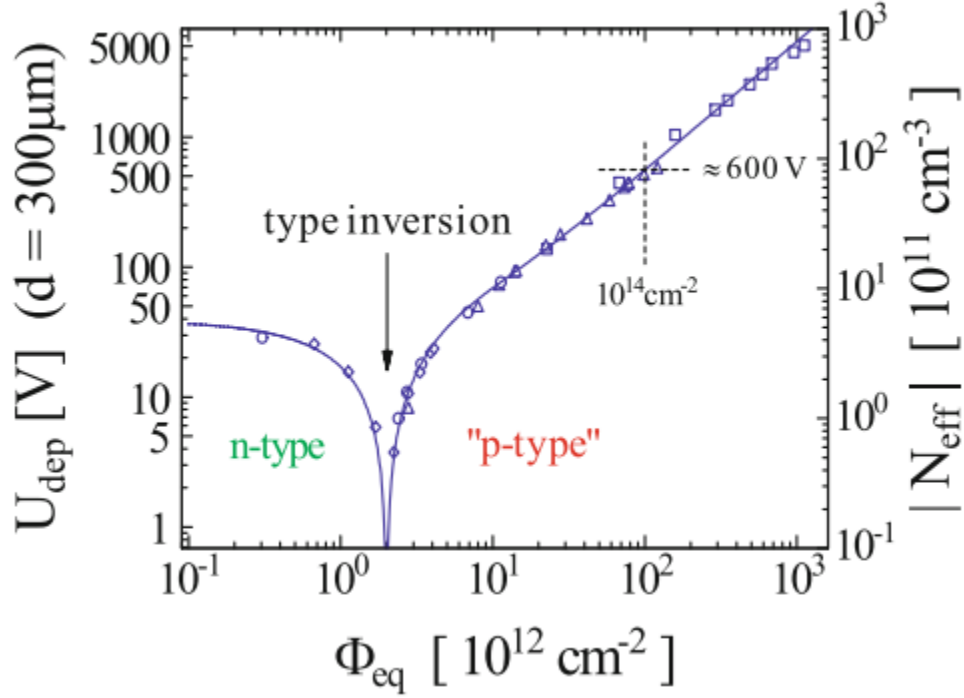


Figure 18. Depletion voltage fluence dependence [10]

The fluence dependence of the trapping centers concentration can be written as Equation 27 [10]:

$$N_i = g_i \Phi_{eq} f_i(t) \rightarrow \tau_{eff} = \gamma \Phi_{eq}, \quad (27)$$

where  $g_i$  is the introduction rate,  $\Phi_{eq}$  is the neutron equivalent fluence of 1 MeV/cm<sup>2</sup>,  $f_i(t)$  is the annealing description of traps with time.

The ratio of the collected charge  $Q$  to the induced charge  $Q_0$  is charge collection efficiency that can be written as Equation 28 [32]:

$$CCE = \frac{Q}{Q_0} = \theta \times \eta = \frac{w}{D} \times \frac{\tau_{eff}}{t_{drift}} \times \left[ 1 - e^{-\frac{t_{drift}}{\tau_{eff}}} \right], \quad (28)$$

where  $\theta$  is a geometric factor,  $\eta$  is a trapping factor,  $t_{drift}$  is carrier transient time. An increase in fluence causes a decrease in CCE as CCE is directly proportional to  $\tau_{eff}$ .

## 2.8.2. Surface defects

Another significant, especially for AC-coupled sensors, type of defects in silicon detectors is surface defects. They are located in the interface between the silicon bulk and the silicon oxide layer (Figure 19) [10]. The distribution of surface defects is not uniform, and the damage is due to the ionization, not the displacements in the atomic structure.

Under the effect of the electric field, electron-hole pairs produced in  $\text{SiO}_2$  layer drift and, depending on the mobility can either escape the layer or can be permanently trapped and form a charge, usually positive, since the mobility of holes is less than electrons. This positive charge induces the negative one in the silicon bulk at the interface which affects several device parameters. In order to diagnose and investigate the surface damage, one can measure the flat-band voltage.

Some surface defects may act like bulk ones. In case the radiation-induced defects are produced at the interface due to the atom displacements or bad wiring. These effects cause surface leakage current but overall are not as significant compared to the bulk ones.

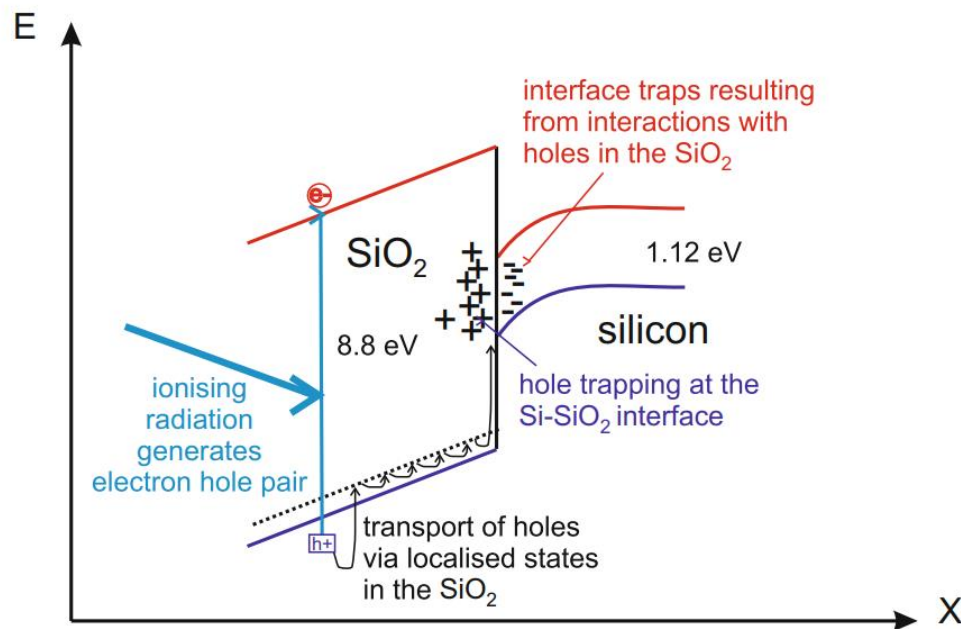


Figure 19. Surface radiation damage in the Si-SiO<sub>2</sub> interface [10]

### 3. EXPERIMENTAL PART

This chapter covers the description and results of the measuring campaign that has taken place at the Nuclear Safety Authority of Finland (STUK).

The measuring campaign had some specific experimental aims:

- Testing the performance of DC-coupled CMS pixel sensors and novel AC-coupled pixel sensors interconnected to the CMS PSI46 ROC under X-rays.
- Obtaining the X-ray spectra from CMS and AC coupled Si detectors for different radiation average energies, tube currents, and voltages.
- Testing the waterproofness and operability of the transparent case developed for water phantom tests.
- Obtaining spectra and hit maps per pixel from a detector in different positions inside the water phantom under the  $^{60}\text{Co}$  source irradiation.

#### 3.1. The experimental setup

During the measuring campaign, the following electronic devices were used as a portable setup:

1. Detectors (CMS DC-coupled Si detector, AC-coupled Si pixel detector) mounted on the PCB
2. Adapter card
3. DTB (detector test board with FPGA)
4. Keithley 6487 Picoammeter/Voltage source
5. Computer with Linux OS and the pXar data acquisition software installed
6. BNC/Lemo and flat band cables
7. USB cable for the DTB

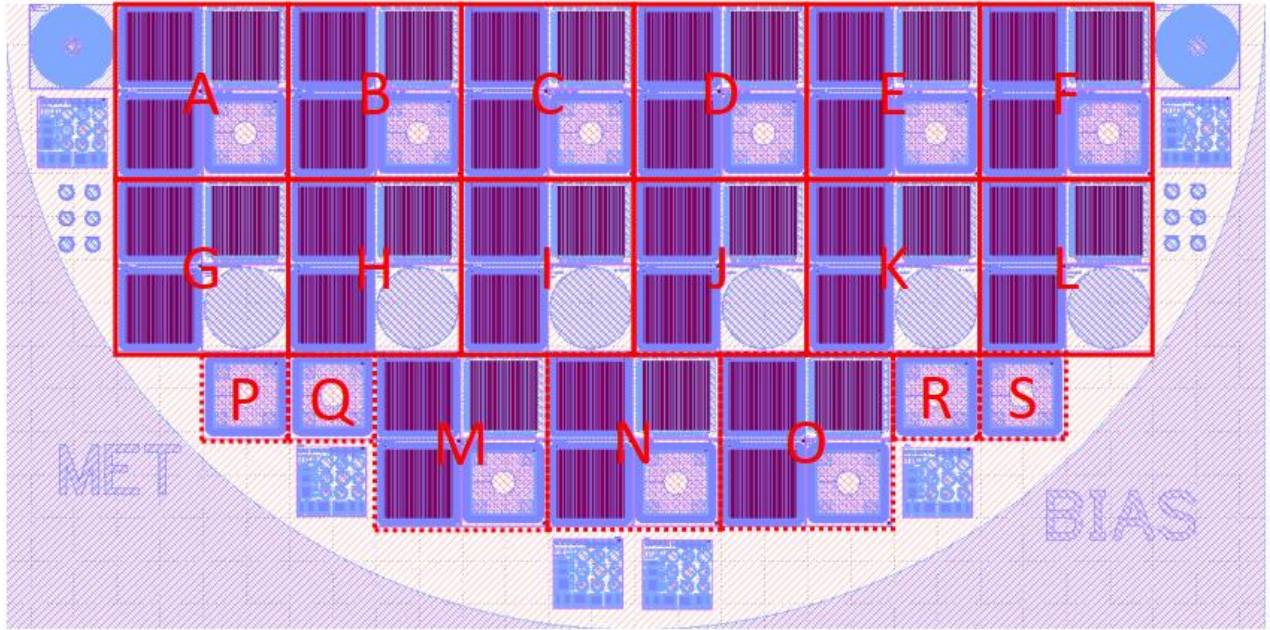
The detectors were tested by using several different radiation sources: an Am-241 source, Isovolt Titan 160 and 320, and a strong  $^{60}\text{Co}$  source Gammabeam X200

manufactured by Best Theratronics (Ottawa, Canada). The 160 kV equipment consists of a Titan E 160 generator and a 160 M2/0.4-3.0 tube housing. The 320 kV equipment consists of Titan E 320 generator and 320/13 tube housing. All additional information regarding the characteristics of the X-ray radiation can be found in Appendix B.

The used detectors are the AC-coupled A1 silicon pixel detector, the AC-coupled pixel detector G1, and the CMS single-chip silicon pixel detector 47A (CMS 47A). The main properties of these detectors are described later in this chapter.

The layout of the AC-coupled A1 and G1 chips on the wafer and the block structure is shown in Figure 20. The letters (A, G) in the name of a detector (single-chip version) are running letters that describe the position of the chip on the wafer. Numbers “1” and “2” mean the different bias line configurations: in the “1”s the bias line is realized by an implant, in the “2”s by an Al metal line on the surface. AC-coupled detectors have 4160 pixels in an  $80 \times 52$  double-column structure, pixels have  $100 \mu\text{m} \times 150 \mu\text{m}$  size to match the CMS PSI46dig read-out chip used in the Phase I pixel detector upgrade. The detectors have an n-in-p structure and were fabricated on magnetic Czochralski silicon substrates [41]. As a dielectric and field insulator, the aluminum oxide  $\text{Al}_2\text{O}_3$  was used, it provides far higher capacitance densities than  $\text{SiO}_2$  due to the high dielectric constant, and more efficient capacitive coupling of pixels [41].

A photo and several microscope images of AC-coupled detectors (with and without bias implant) are shown in Figures 21 - 24. Coupling capacitors and bias resistors connect individual segmented implants to the common bias line in AC-coupled detectors.



## Block structure

Each block contains:

- AC coupled pixel, bias line implant
- AC coupled pixel, no bias line implant
- RBI-HIP CdTe DC coupled pixel
- EITHER diode OR MOS capacitor

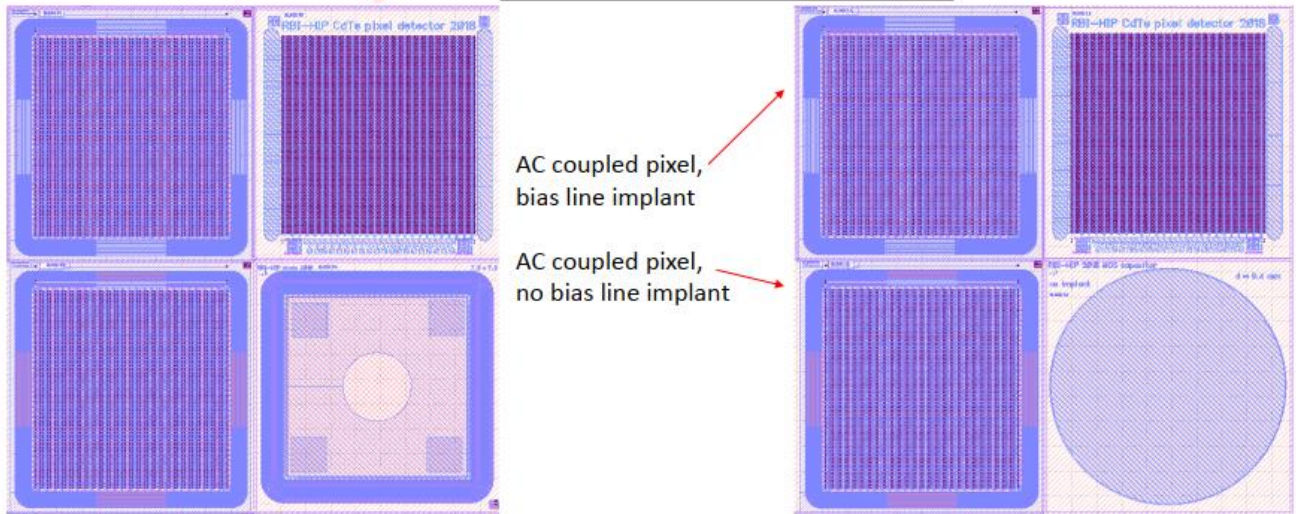


Figure 20. Wafer and block structure with the AC-coupled A1 and G1 silicon pixel chips [40]

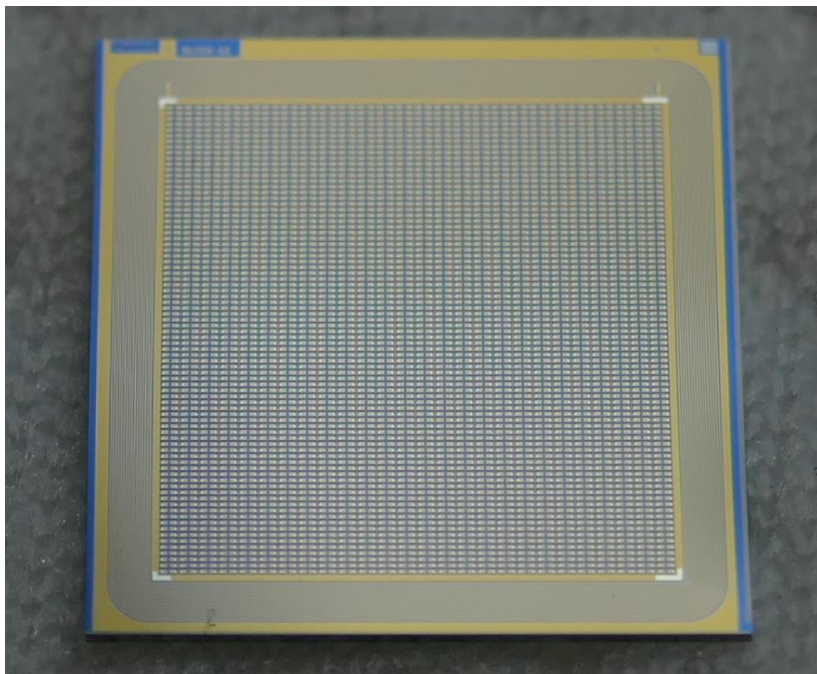


Figure 21. A photo of the AC-coupled single-chip detector [HIP CMS Upgrade project]

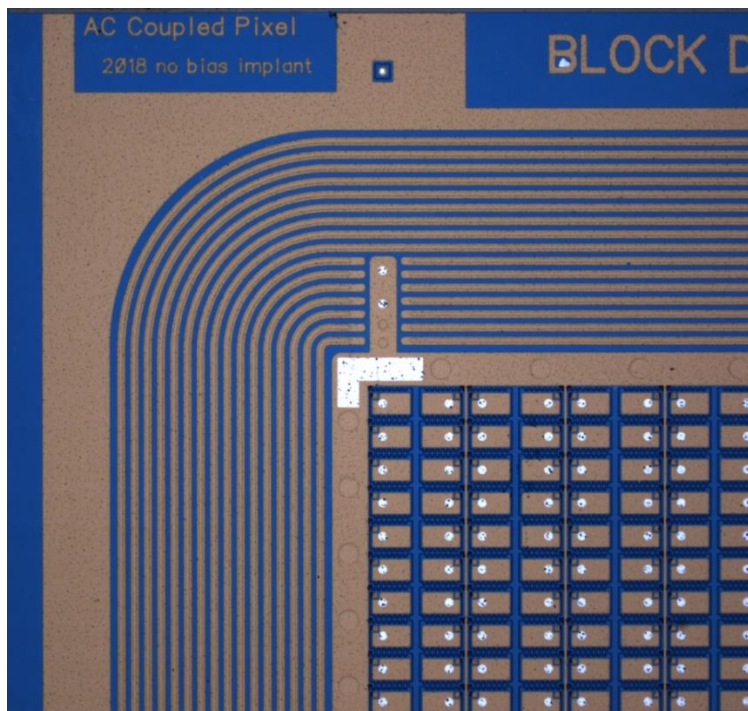


Figure 22. A microscope image of AC-coupled pixel detector with no bias implant [HIP CMS Upgrade project]

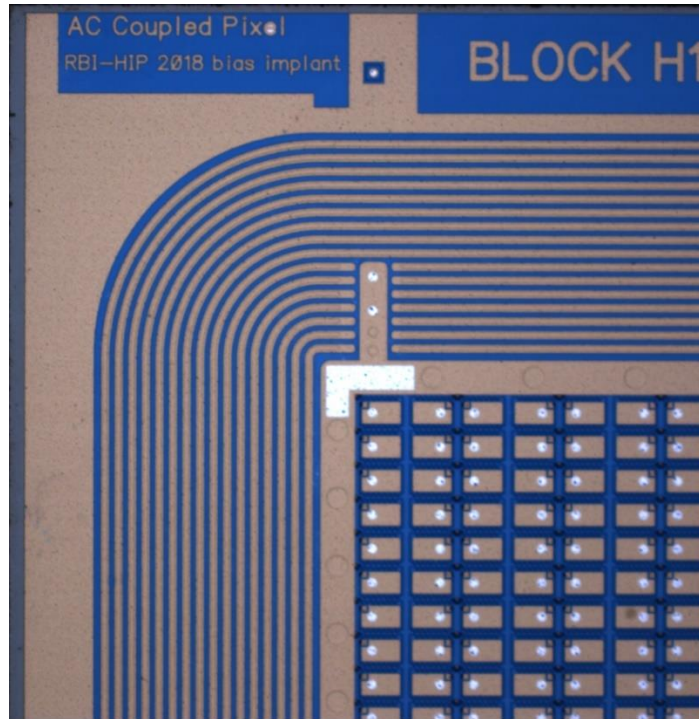


Figure 23. A microscope image of AC-coupled pixel detector with the bias implant [HIP CMS Upgrade project]

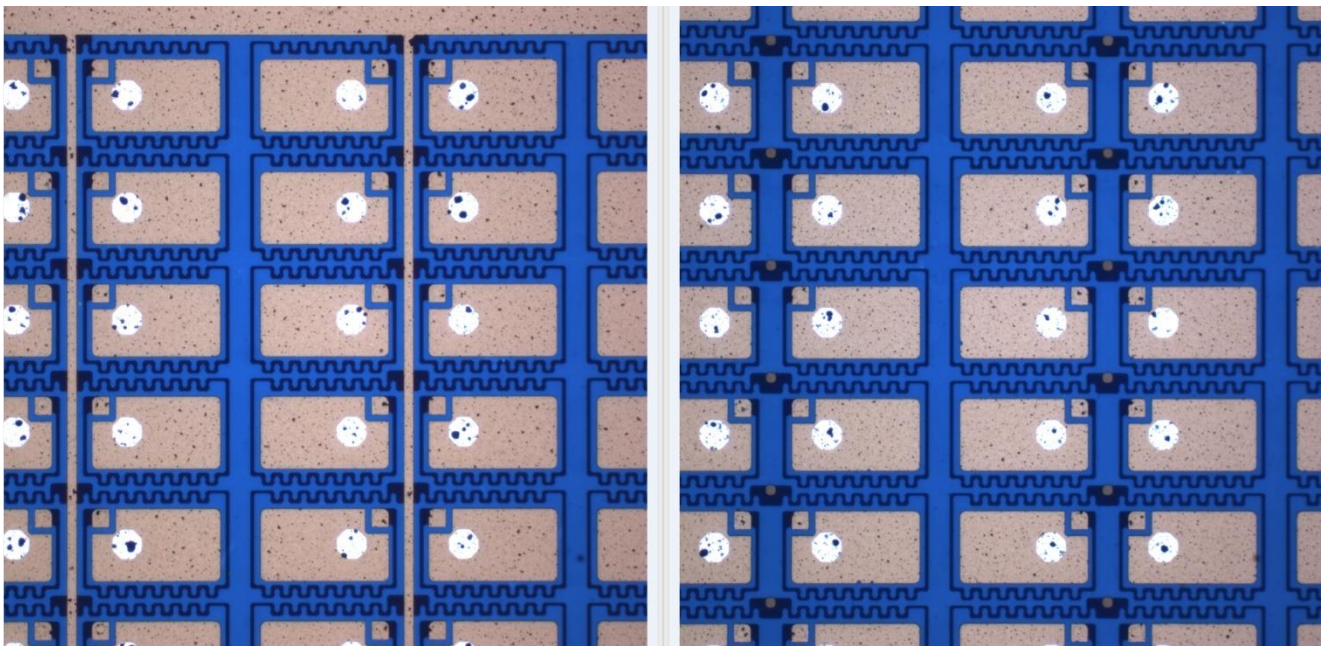


Figure 24. Microscope images of detectors without the bias implant (on the left) and with the bias implant (on the right) [HIP CMS Upgrade project]

### 3.2. X-ray box test

The AC-coupled A1 silicon pixel detector was irradiated with a small Am-241 source inside an isolated X-ray box, Measurements were carried out by almost the same portable setup that was listed before. A detailed description of the hardware including DTB is given in [35]. To qualify pixel modules one has to run a specific suite of tests that is called the FullTest. The FullTest is a sequence of the following tests:

- PreTest
- PixelAlive Test
- Trimming Test
- PHOptimization Test
- GainPedestal Test

The methodology and outputs for these tests are comprehensively described in [36]. PreTest ensures the functioning state of the ROC by configuring the Digital-to-Analog Converter (DAC). PixelAlive Test sends an input signal to check if all pixels respond to it. Trimming is very important, by applying the additional supply voltage to the comparator to decrease the threshold, it sets all pixels to turn on with the input signal of the same strength. PHOptimization Test optimizes the dynamic range of the output pulse heights. GainPedestal measures and stores the gain and pedestal of each pixel and checks the linearity of the Analog-to-Digital Converter (ADC) response [36].

After the FullTest was performed for the A1 detector, a small Am-241 source was put inside the X-ray box. Figure 25 presents the 2D histogram of the PixelAlive Test, and Figure 26 presents the hitmap under the Am-241 source radiation. Further, the scale to the right of the histograms is the number of entries per pixel detected.

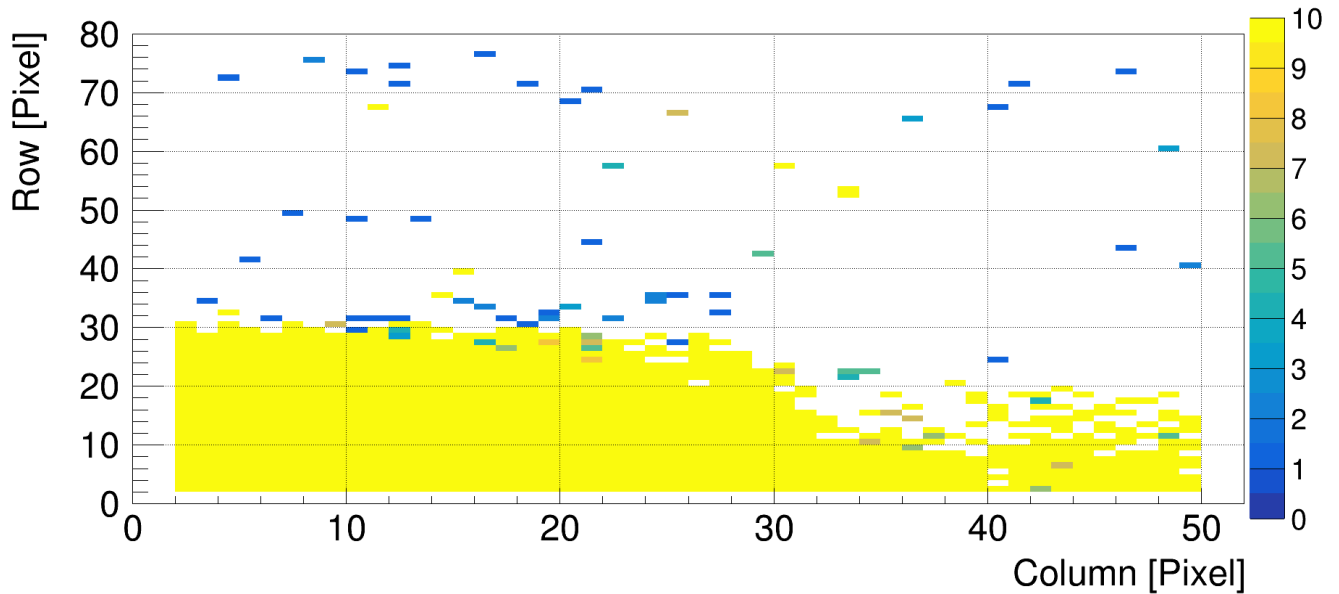


Figure 25. The 2D histogram of PixelAlive Test results for the A1 detector

All the colored pixels are meant to be responsive and give feedback when the detector is exposed to the radiation source. But the actual measurements had opposite results. The hit map under the radiation from the Am-241 source is shown in Figure 26, all colored pixels are responsive. The PixelAlive Test marked them as “dead” and vice versa the marked as “alive” pixels are non-responsive. Even for different trimming voltage values, the outcome regarding the responsiveness was the same, but as a side effect higher trimming voltages leads to less precise measurements energy-wise. The reason for such results is yet to be discovered. It might be due to the readout electronics failure. This can be proved with the mean X and Y coordinate values for the registered events. For the PixelAlive Test the mean X value is 20.92, Y is 13.91, while for the hitmap the mean X is 24.49, mean Y is 63.73.

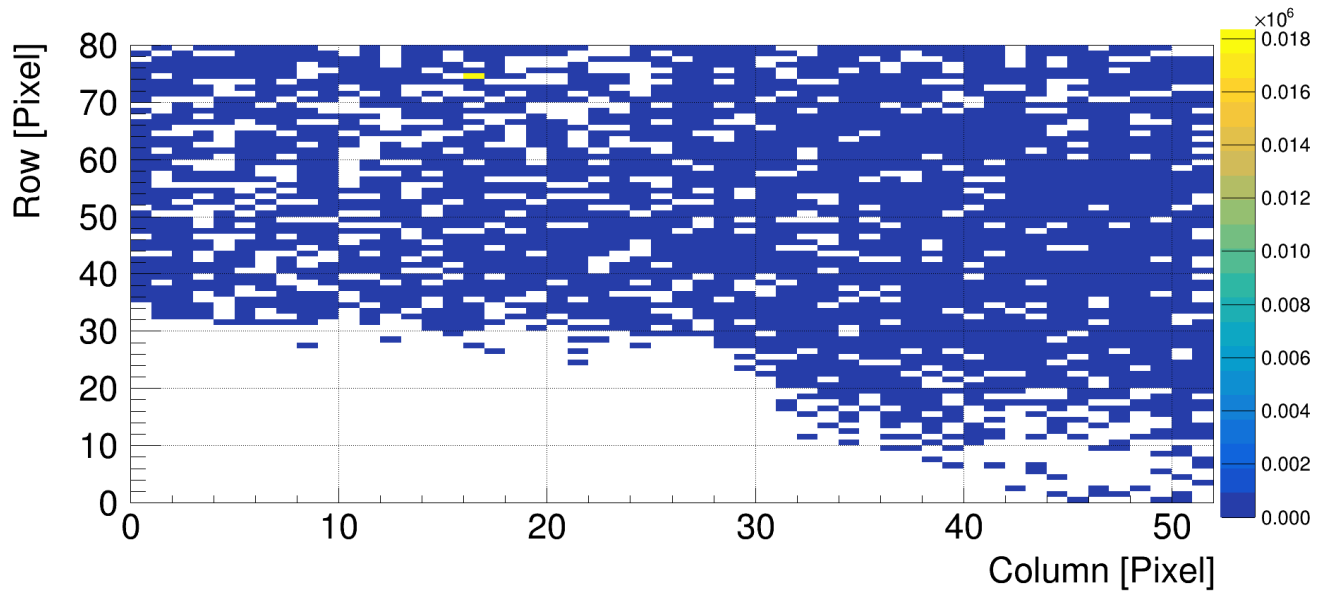


Figure 26. The hitmap of the A1 silicon pixel detector under the Am-241 source radiation

Two yellow pixels that can be seen in Figure 26 are so-called “hot” pixels. These pixels false trigger the particle hit resulting in high noise peaks on the energy spectrum. They can be masked and will not contribute to the resulting characteristics.

### 3.3. X-ray tube tests

The layout for the runs with different X-ray tubes is shown in Figure 27, where the X-ray sources, the detector inside a black plastic box that shields it from light and electrostatic discharge ESD (more closely in Figure 28 a), and the DTB shielded from the incident radiation by lead bricks can be seen. The tube with a rotatable filter array is shown in the background as well. The distance between the X-ray tube and the detector was 2 meters throughout the whole experiment, the position of the detector in space relative to the beam was determined using lasers, the table height and placement could be adjusted with a remote control device (Figure 28 b).

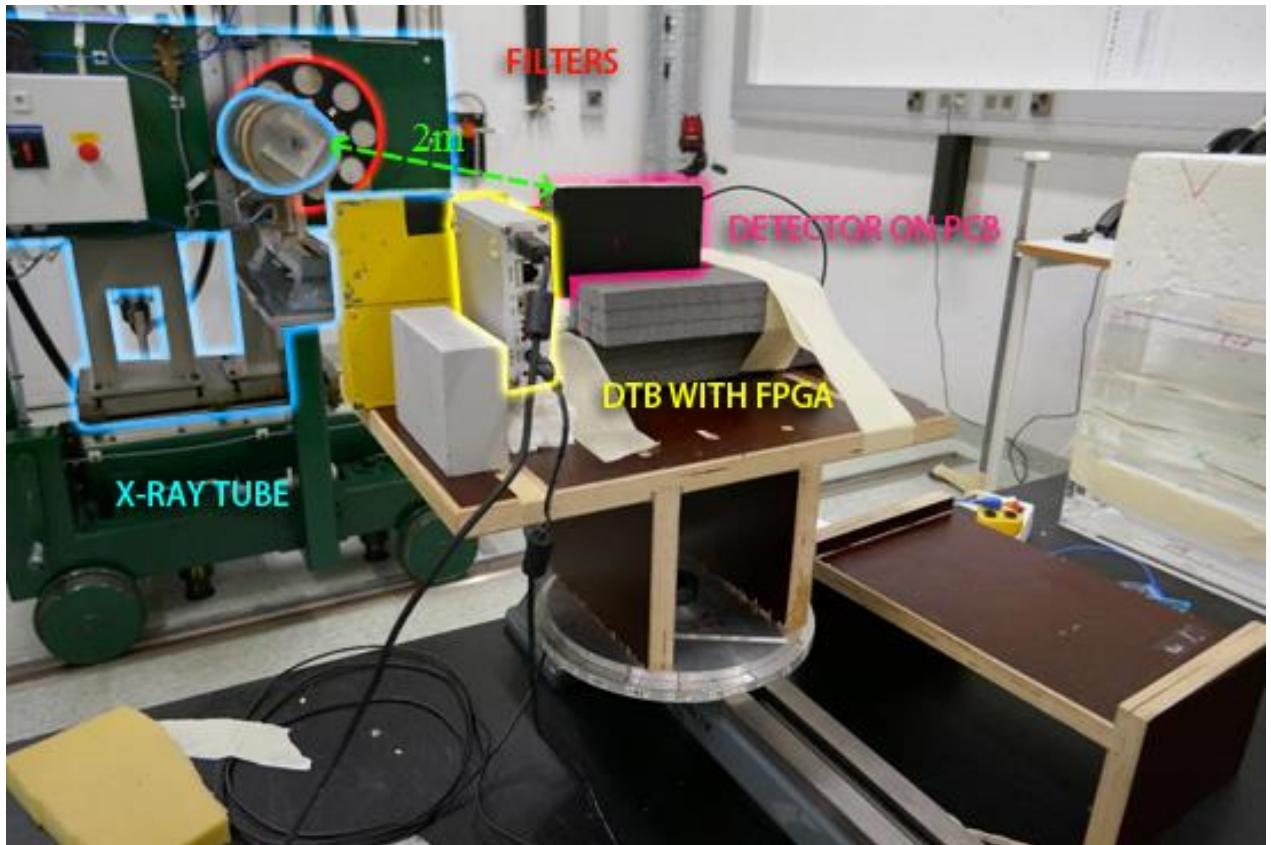
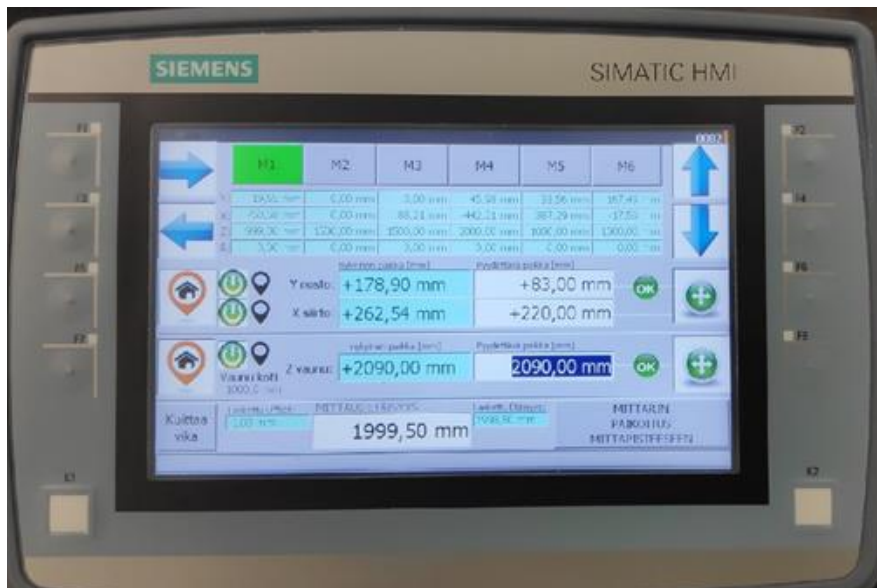


Figure 27. The setup with X-ray tubes

The detector, due to the setup features, was facing the wall, so the X-rays had to penetrate the plastic box and the PCB on which the detector was mounted. This will be fixed for the future tests, the box and connections will be reorganized, and the opening in the plastic will be made and covered with aluminum foil.



a)



b)

Figure 28. a) Close picture of the detector inside the black plastic box and the DTB shielded by lead bricks, b) Remote control device with table placement information

Two types of X-rays were used during the X-ray tube tests: the ISON narrow and the RQR broad X-rays.

The ISON series provides X-rays with relatively narrow energy distribution, due to additional filtering which reduces the continuum X-rays at lower energies. This radiation quality is used for initial tests of the detectors, e.g. to select a suitable beam

current, and is employed to assess the energy dependence of the detector response. The key parameters of the ISON X-ray quality series are presented in Appendix B (Table B1).

The X-rays of the RQR series resemble clinical radiation beams of conventional X-ray and CT devices, with a broad continuum spectrum at lower energies complemented by characteristic X-rays at sufficiently high tube voltages and currents. The RQR series can give more information to study the performance of used AC-coupled G1 and CMS 47A silicon pixel detectors and data analysis algorithms under more realistic conditions. The key parameters of the RQR X-ray series are presented in Appendix B (Table B2).

### **3.3.1. X-ray tube tests with AC-coupled silicon pixel detector G1**

AC-coupled pixel detector G1 from Wafer 2 of the HIP-RBI Pixel2018 production was used. HIP-RBI Pixel2018 is a detector processing run done in Micronova by the HIP group. The bias voltage is -40 V, trimming settings at 120 Vcal were adapted at some point to mask new noisy pixels. The journal with recorded runs is presented in Appendix A. The “filltree” refers to the functionality of the readout to record position information for each event, i.e. effectively pixel-by-pixel spectra. This was not applied in all runs because the time needed for one measurement significantly increases with the filltree.

Some parameters values like room temperature and relative humidity (RH) were obtained for each run to make sure there will be no unexpected changes in results. For the G1 tests, the temperature was 20.4 °C, RH was 46.2 %.

Only narrow X-rays were used for the G1 detector tests. Shown in Figure 29 energy spectrum have its peak shifted for different radiation qualities. It corresponds to the per bin info of the fluence spectra by the means of peak shifting with increased average

energy, however, the method for determining the actual fluence has some uncertainties. The spectra have been measured with a germanium detector. From the measured spectra, the fluence is calculated with a simulated response of the detector. The method for calculating the fluence is described in STUK publication TR-30 [37]. With the increase of average energy the number of registered hits increases.

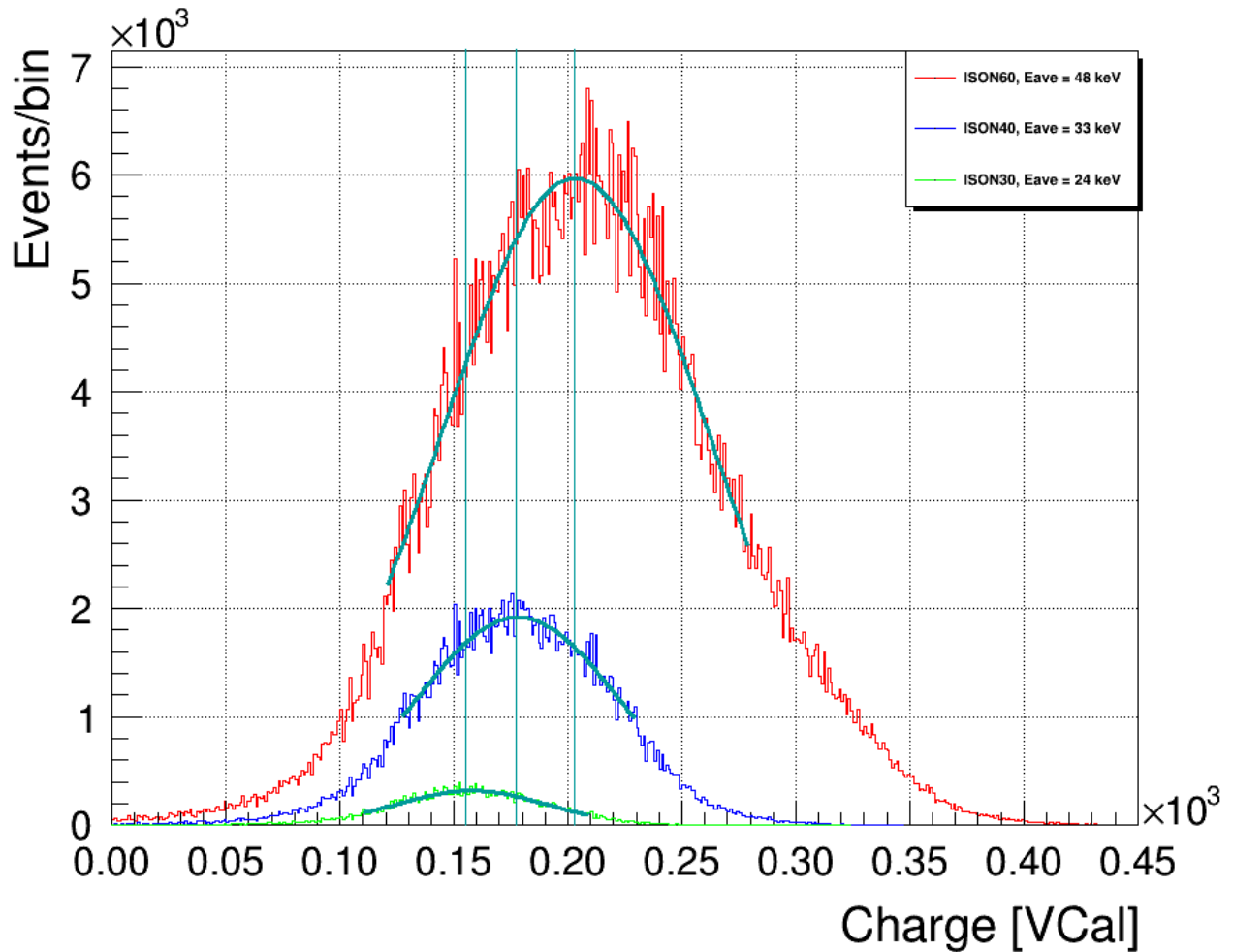


Figure 29. Spectra of narrow X-rays measured with AC-coupled silicon detector G1

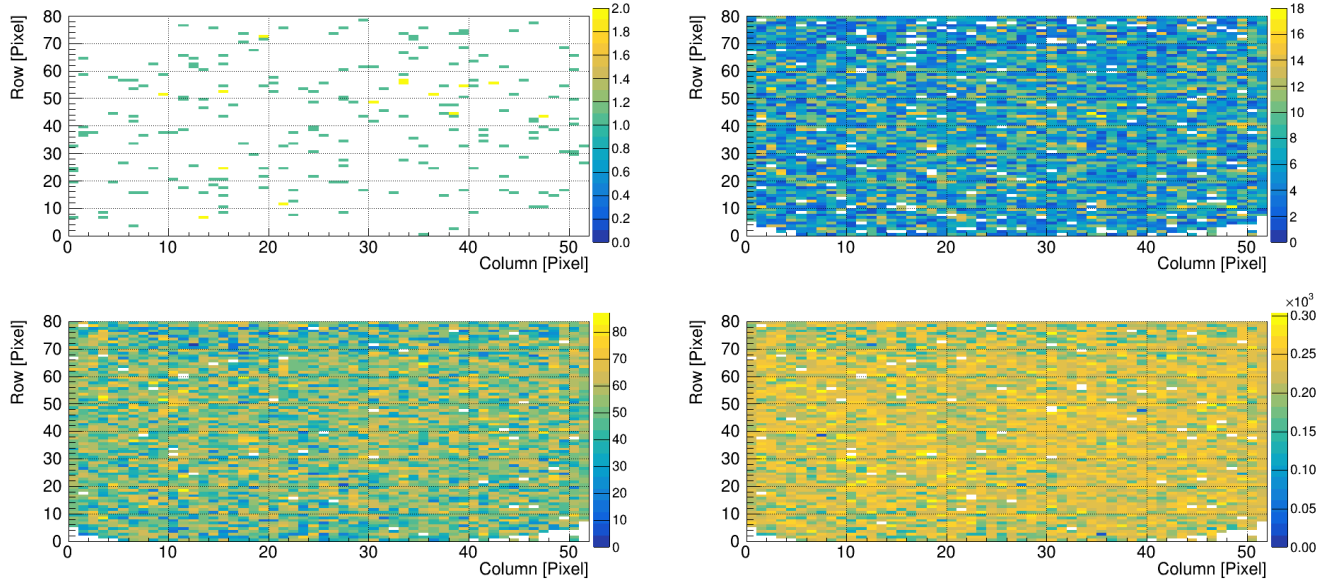


Figure 30. Hitmaps of the AC coupled pixel detector G1. The top left is a noise hitmap without any radiation sources. The top right is a hitmap for the ISON30 X-rays, the bottom left is for the ISON40 X-rays, and the bottom right is for the ISON60 X-rays

### 3.3.2. X-ray tube tests with CMS single-chip silicon pixel detector 47A

As was mentioned in Chapter 2 the single-chip variation of pixel modules that were built into the CMS pixel tracker during the phase 1 upgrade has  $80 \times 52$  pixels with  $100 \mu\text{m} \times 150 \mu\text{m}$  size, these pixels are bump bonded to the PSI46dig readout chip. The pixels use the n+-in-n type design and were done by the CiS company in Eastern Germany. This single-chip detector was tested under narrow ISON and broad RQR X-rays. According to the journal, measurements started with runs that were made with ISON-30 X-rays from the 160 kV X-ray tube irradiating the detector. Several runs with varying tube current were made, the results are shown in Figure 31, Figure 32, and Figures 33, 34 for the long filltree run.

The CMS 47A silicon pixel detector was tested under X-rays of different radiation energies and beam currents. The bias voltage was set to -150 V. At first, the detector was

trimmed for 35 Vcal, but the PixelAlive Test shown too much irresponsive hot pixels (around 200), therefore, detector trimming voltage was increased from 35 to 50 Vcal. Detector trimmed for 50 Vcal had only two bad pixels that were masked (19:6 and 25:66). For the CMS 47A tests, the temperature was 20.2 °C, RH was 46.5 %.

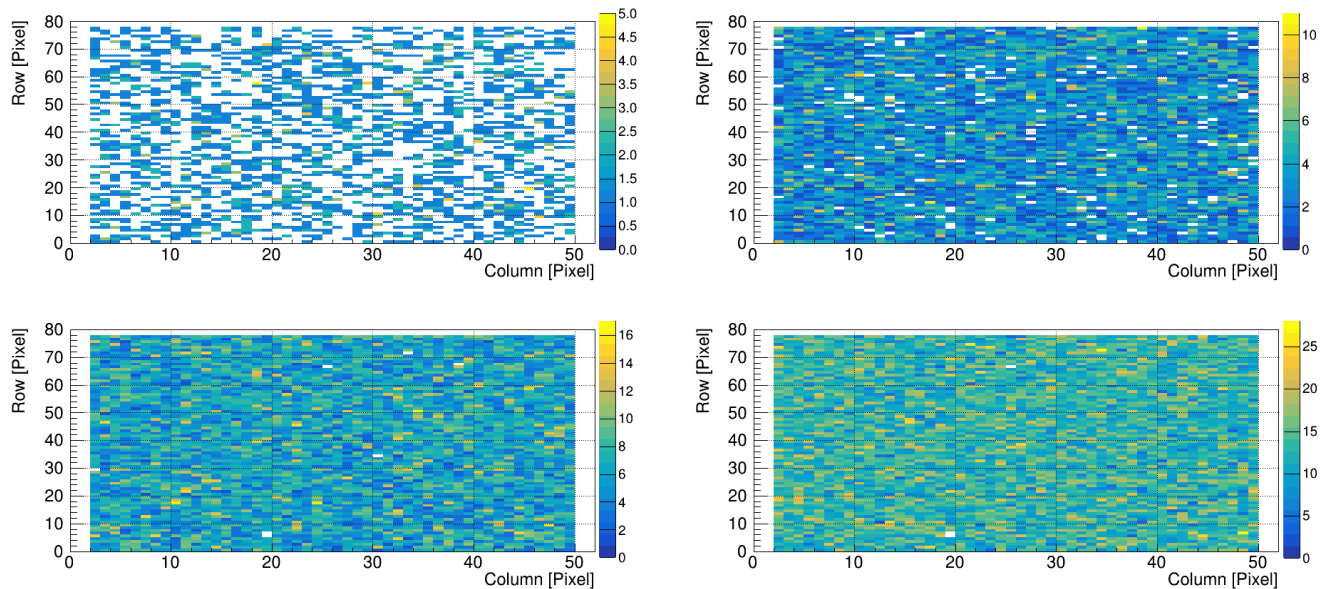


Figure 31. Hitmaps of the CMS 47A silicon pixel detector. The top left is hitmap for the smallest tube current 1 mA, the top right is a hitmap for 5 mA, the bottom left is for 10 mA, and the bottom right is for 20 mA

The increase in tube current leads to a larger amount of registered particle hits. The color of the pixel is yellow when it registers a large number of events, as the tube current increases, the color scheme becomes more yellow. With high intensities, each pixel registers more events including side effects like charge sharing and pile-up. Charge sharing happens when one pixel gets hit by a high energy particle and the charge is shared to a pixel that did not get hit. Due to that charge the once empty pixel fires and sends the signal to the readout electronics. In case of pile-up, a pixel gets hit by two or more particles, and due to slow readout electronics, such an event is registered as one hit. It is

impossible to separate the more-than-one photons, so the total energy is a sum of energies of those incoming particles. The non-piled up image can be reproduced using specific software solutions including clustering and forming the event-by-event data. At this stage of research, the event-by-event data would not give much more information, so this could be implemented in future test campaigns.

The spectra initially have VCal as the X-axis unit, but to make them more clear a normalization algorithm was made and successfully implemented. To convert VCals to eV the following relation was used (Equation 29):

$$eV = VCal \cdot V_{trim} \cdot 3.6, \quad (29)$$

where  $V_{trim}$  is the trimming voltage; on average, Si produces one electron-hole pair for every 3.6 eV particle crossing the medium releases.

The trimming voltage sets a coarse-scale for the trimming (as a ROC-wide value) and reduces the signal amplitude required to fire the comparator. The normalization was applied concerning the average radiation energy values for different radiation qualities (narrow and broad). This normalization algorithm can be applied only for the spectra obtained with a detector trimmed for 50 V. The normalization has to be reconsidered when the trimming value is changed. However, during this test campaign, the CMS 47A silicon pixel detector was trimmed once for 50 V and, therefore, the spectra obtained during the X-ray tube runs can be normalized.

With an increase in the tube current, the detector registers more events, however, the mean peak does not shift. The Gaussian fits were made by coding a script with the data analysis framework ROOT commands.

The long filltree run presented in Figure 33 and Figure 34 resulted in higher energy resolution. An optimal tube current for other measurements was chosen equal to 20 mA. This tube current was high enough to obtain a significant number of entries while keeping the number of negative side effects and noise level relatively slow.

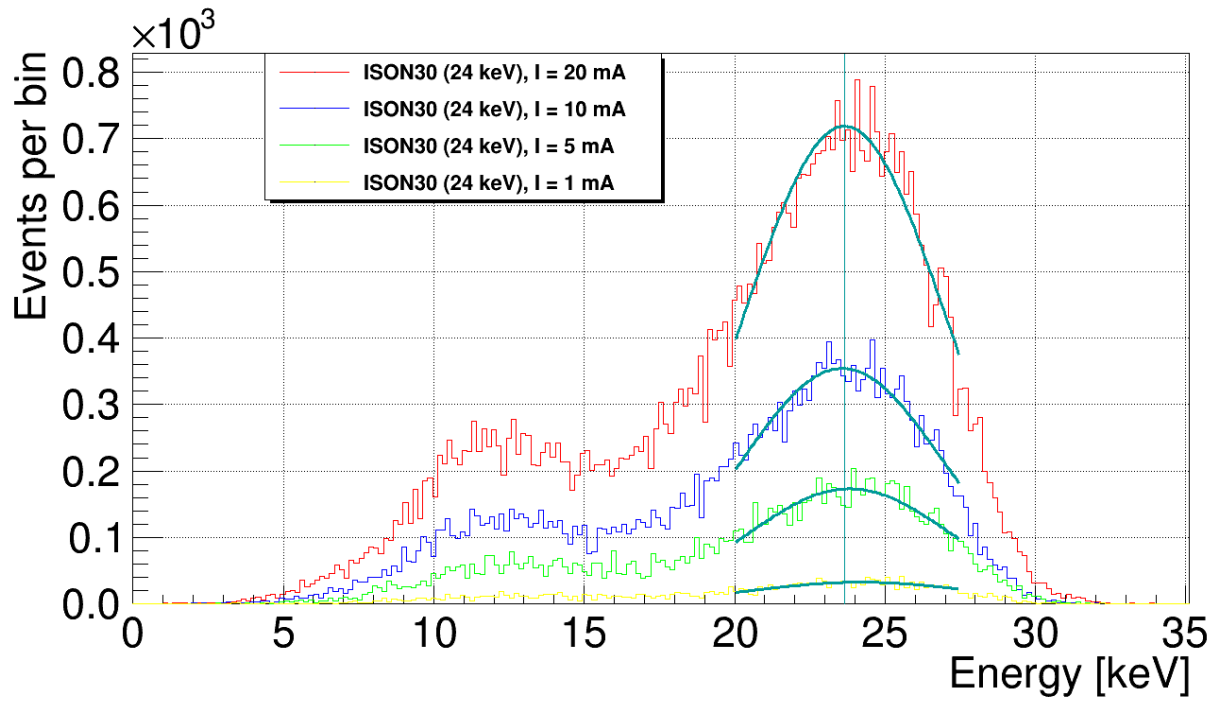


Figure 32. Spectra measured for different tube currents with ISON-30 radiation quality

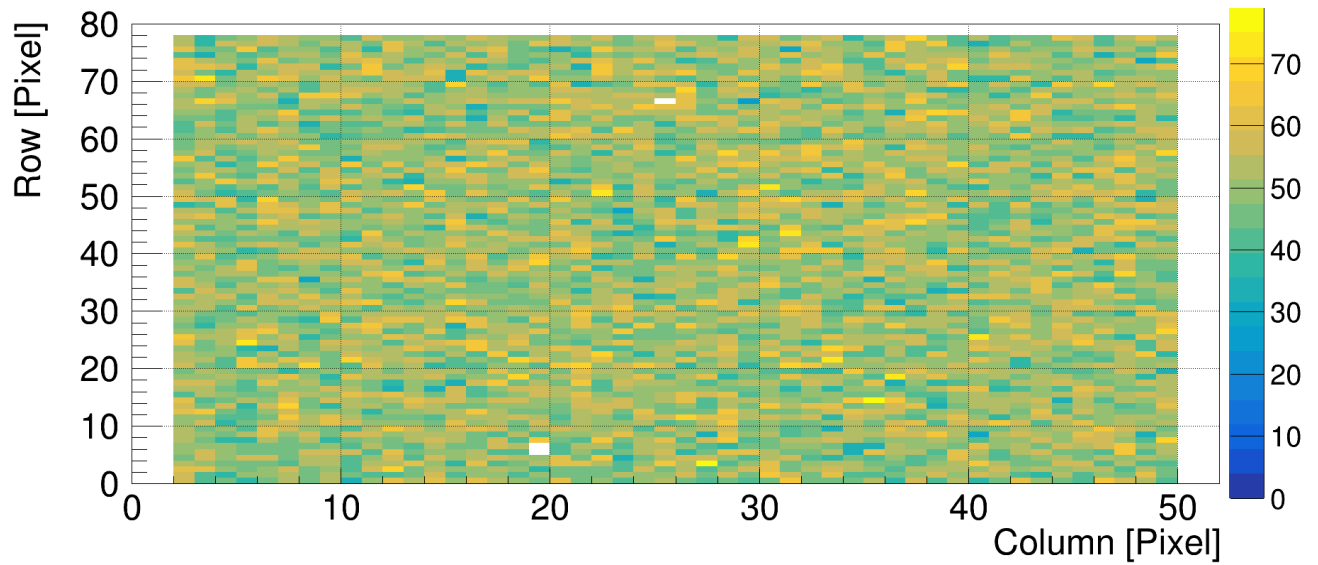


Figure 33. Hitmap for the long filltree run with the ISON-30 radiation quality

The second peak observed at lower energies on the spectrum can be a sum of noises caused by various X-ray-matter interactions registered by the CMS 47A and a small peak around 12.5 keV that can be observed in Figure 31 [37].

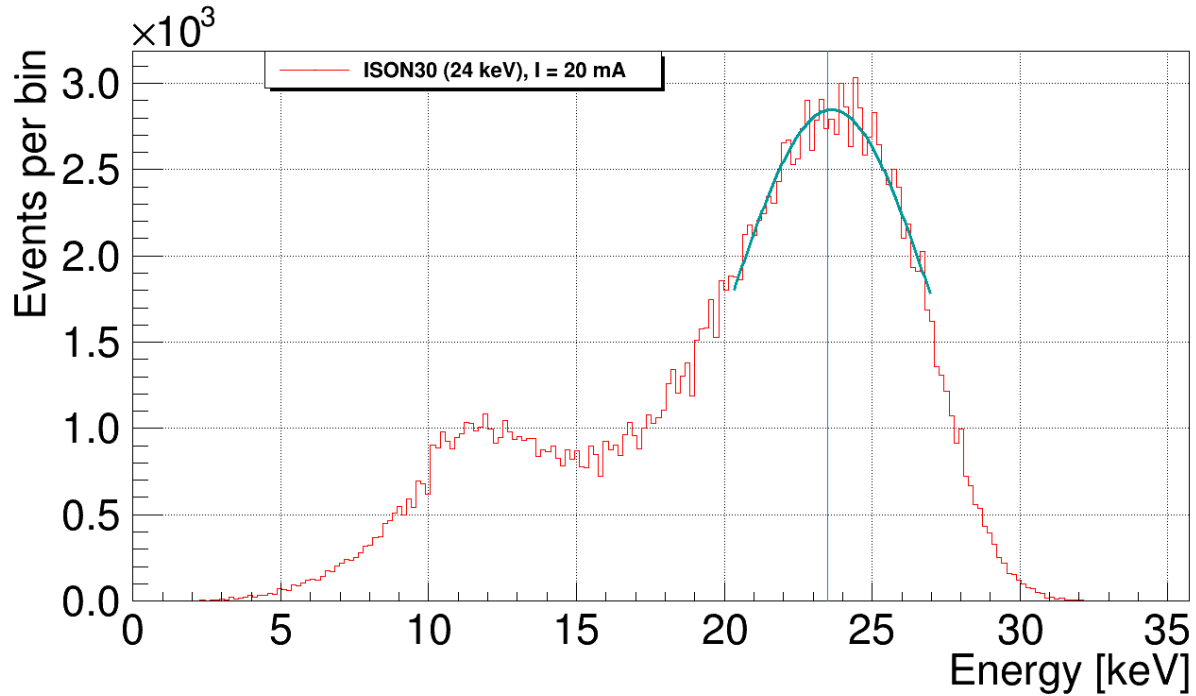


Figure 34. Spectrum measured for 20 mA with the ISON-30 radiation quality (filltree)

Further measurements for narrow X-rays were performed with a 320 kV X-ray tube. For the ISON-80 and the ISON-100 radiation qualities the hitmaps (shown in Figure 36) and energy spectra (shown in Figure 37, 38) and were obtained.

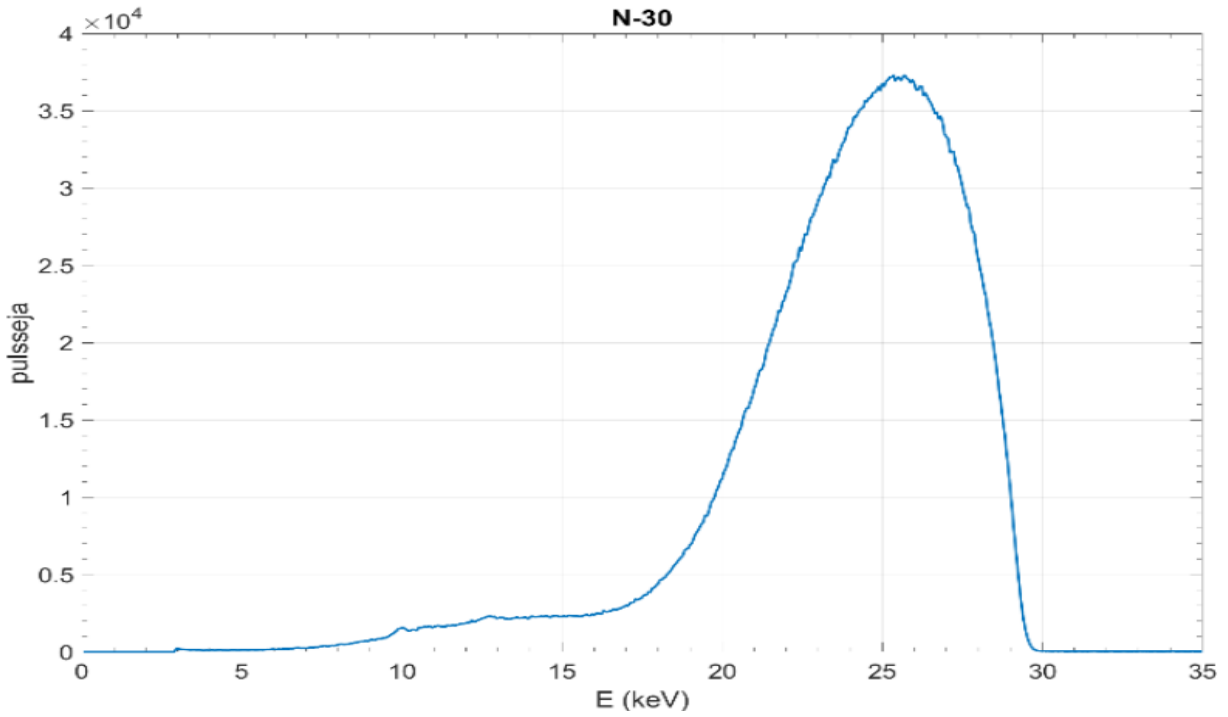


Figure 35. Fluence spectrum of the ISON-30 radiation quality[37]

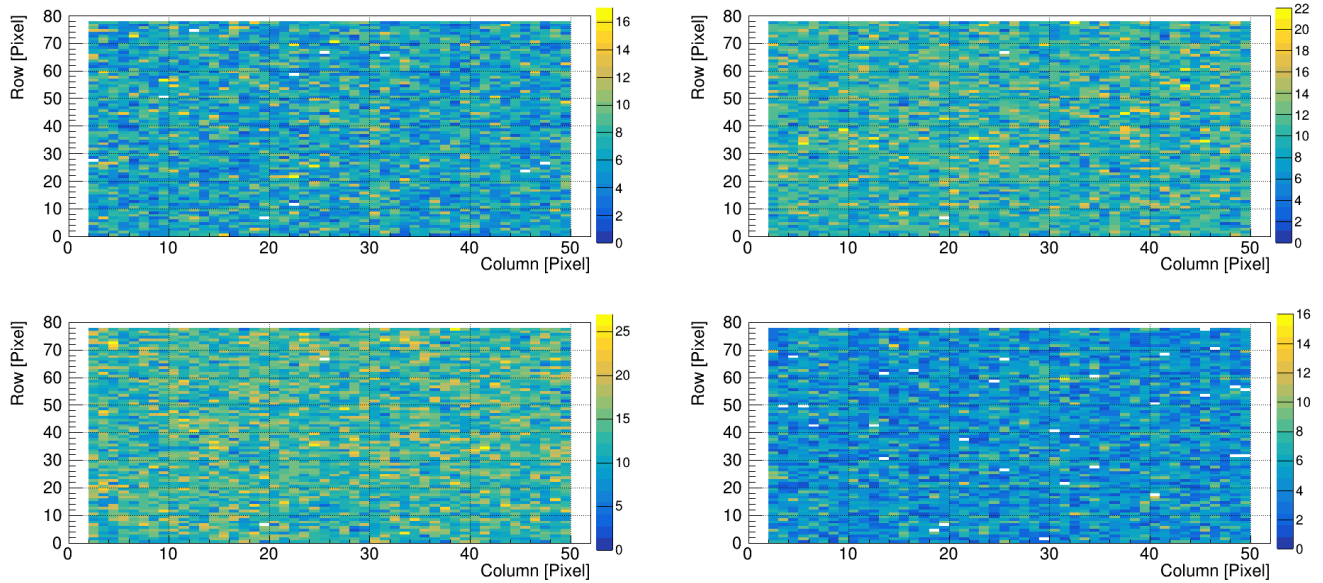


Figure 36. Hitmaps of the CMS 47A silicon pixel detector. The top left is a hitmap for the ISON-80 with 20 mA tube current, the top right is a hitmap for the ISON-80 with 30 mA tube current, the bottom left is a hitmap for the ISON-80 with 40 mA tube current, and the bottom right is a hitmap for the ISON-100 with 20 mA tube current

As shown in Figure 36 the hitmap for the ISON 100 radiation quality has fewer registered entries which correlates with the measured spectrum. The tube current for the ISON-100 was 20 mA. Even though the average energy is higher for the ISON-100 (83 keV) compared to the average energy for the ISON-80 (65 keV), the number of registered entries is less for the ISON-100, even though the tube current was the same.

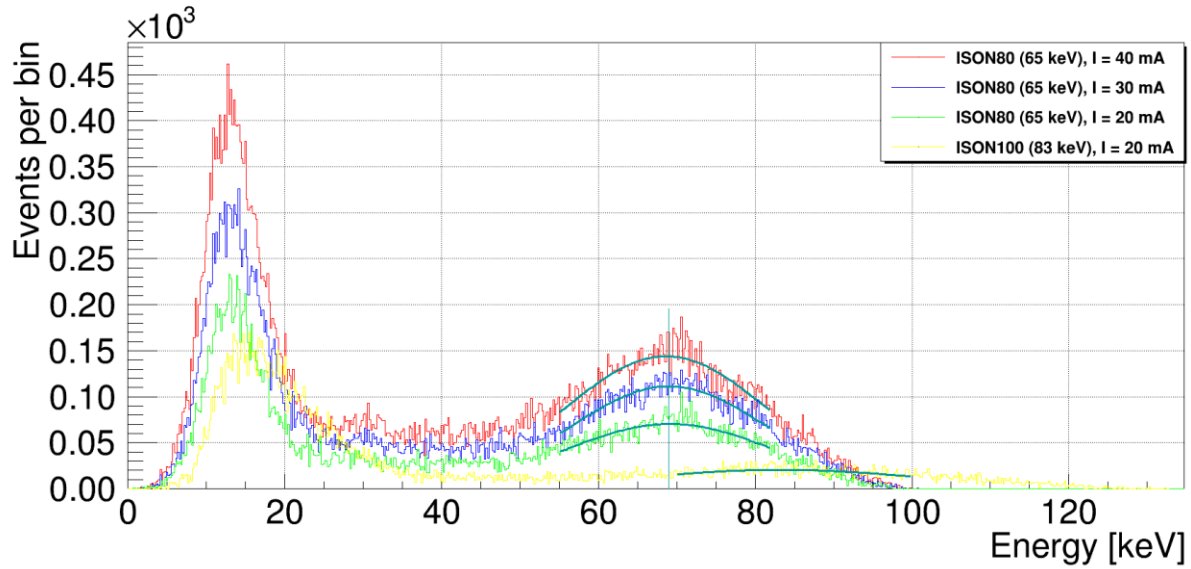


Figure 37. Spectra measured for the ISON-80 and the ISON-100 radiation qualities

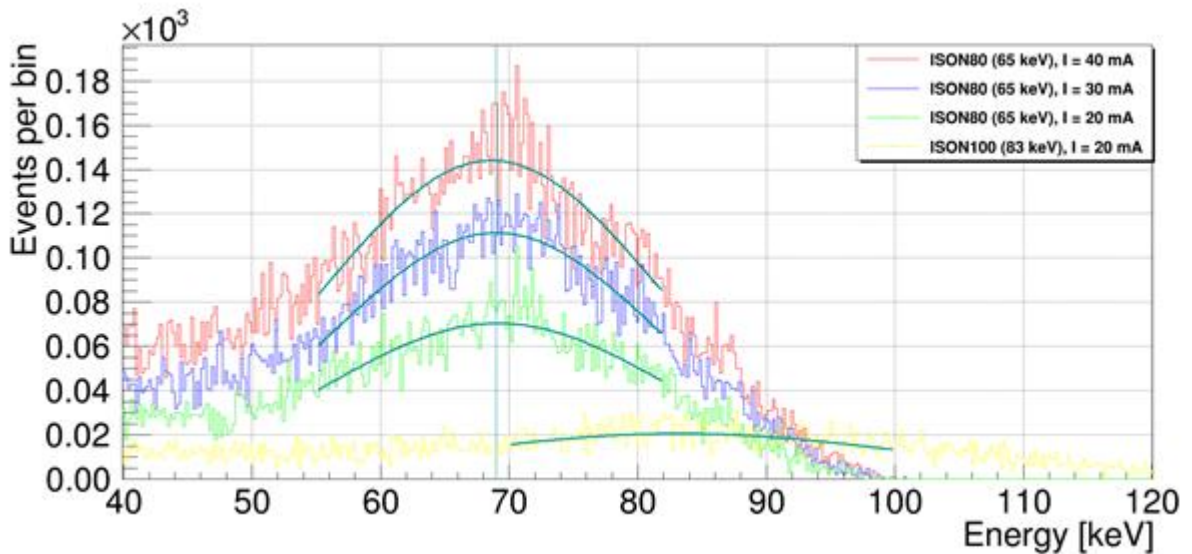


Figure 38. Closer picture of X-ray peaks

The higher the energy, the more “transparent” the pixel detector becomes for the ionizing radiation. In addition, Si has low Z-number and the device is only around 300  $\mu\text{m}$  thick.

The peak for the ISON-80 runs is not shifted, the number of events per bin increases with larger tube currents.

The spectra for the ISON-80 with tube currents 20 mA and 30 mA have high noise levels which makes it harder to analyze. The reason for the noise is naturally scattering from other materials presented in the room.

The following measurements were done for broad X-rays (RQR series). First, to investigate the effect of the change in tube current, two RQR-2 runs (shown in Figure 39) with different currents 10 mA and 20 mA were performed.

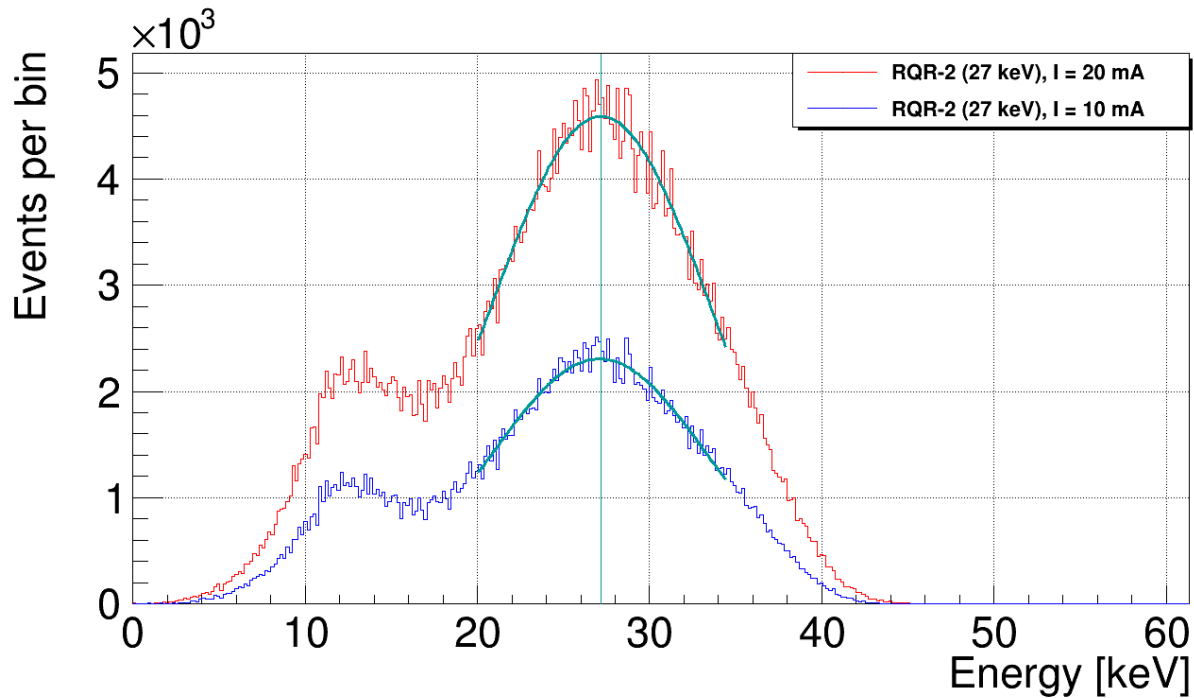


Figure 39. Spectra measured for the RQR-2 radiation quality with two tube currents 10 mA and 20 mA

The spectrum for the RQR-2 with tube current 20 mA has more events and therefore is optimal, in the case of 10 mA tube current run, the peak is broader, there is no shift in peak observed.

The next step was to test broad X-rays with different radiation qualities (RQR-2, RQR-4, RQR-6). The results are shown in Figure 40 and Figure 41.

Measured spectra have low energy noise which does not correspond to the fluence spectra. A possible reason might be that the detector response affects the spectrum shape including detection efficiency and Compton continuum. Also, the presence of the additional material (cover and the PCB) may cause scattering.

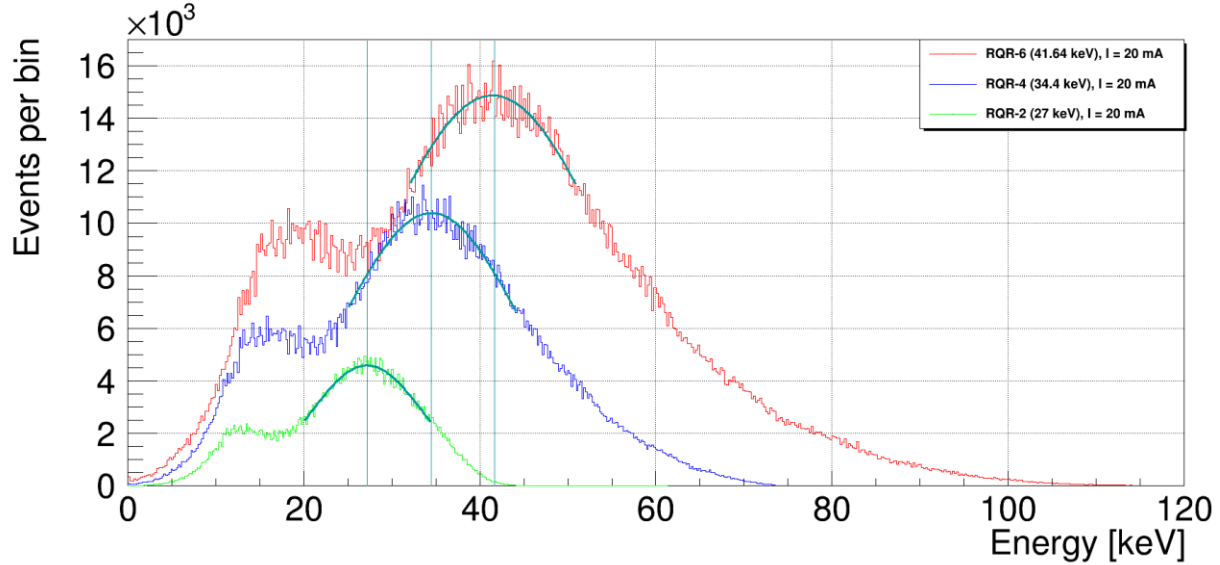


Figure 40. Spectra measured for different radiation average energies of RQR series with tube current 20 mA

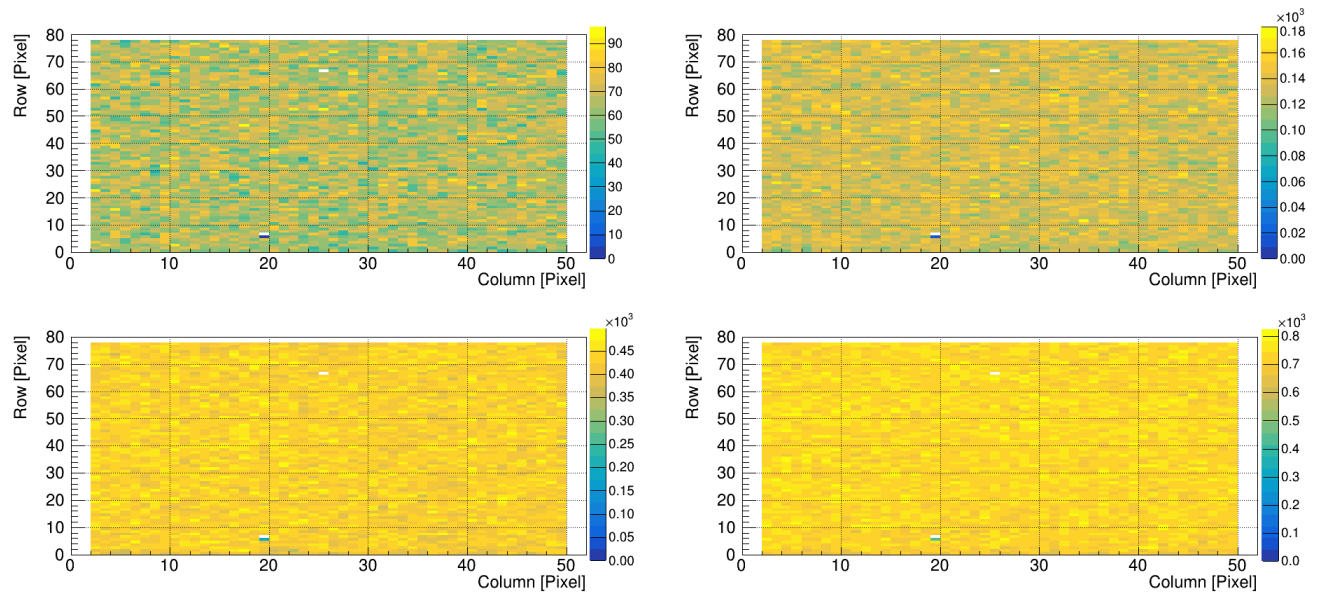


Figure 41. Hitmaps of the CMS 47A silicon pixel detector. The top left is a hitmap for the RQR-2 with 10 mA tube current, the top right is a hitmap for the RQR-2 with 20 mA tube current, the bottom left is a hitmap for the RQR-4 with 20 mA tube current, and the bottom right is a hitmap for the RQR-6 with 20 mA tube current

The influence of these effects can be calculated with detector response simulations. Furthermore, there might be problems with measurements or data analysis tools. Multiple oddities like the shift of the spectrum endpoint when the fluence is increased take place. The pileup effects might be a reason. A closer look at the data analysis script and the functionality of the ROC with some additional measurements will be made during future research campaigns.

### 3.4. $^{60}\text{Co}$ test with the water phantom

The setup and the readout chain for the  $^{60}\text{Co}$  tests are very similar to the one described in Section 3.1. The detector with an adapter card was inserted into a custom-milled transparent plastic box (Figure 42) that was modified from the previous underwater test campaign. New o-ring and layers of Teflon tape around the cable opening

were added for better leak protection since the preliminary short tests showed small leakage. The water tightness was verified without the detector inside. A round cable replaced the short ribbon cable as a connector between the adapter card and DTB. The box with the detector was lowered into the water phantom, which represents the human body, which is mostly water, clamped to the round cable. The position of the detector relative to the beam source was changed between runs within the water phantom.

For the CMS single-chip Si pixel detector underwater tests, the bias voltage was -150 V. Leakage current before irradiation was measured and had a value of 0.095  $\mu\text{A}$ . Measurements of the leakage current were made for each run and presented in Appendix A (Table A3).

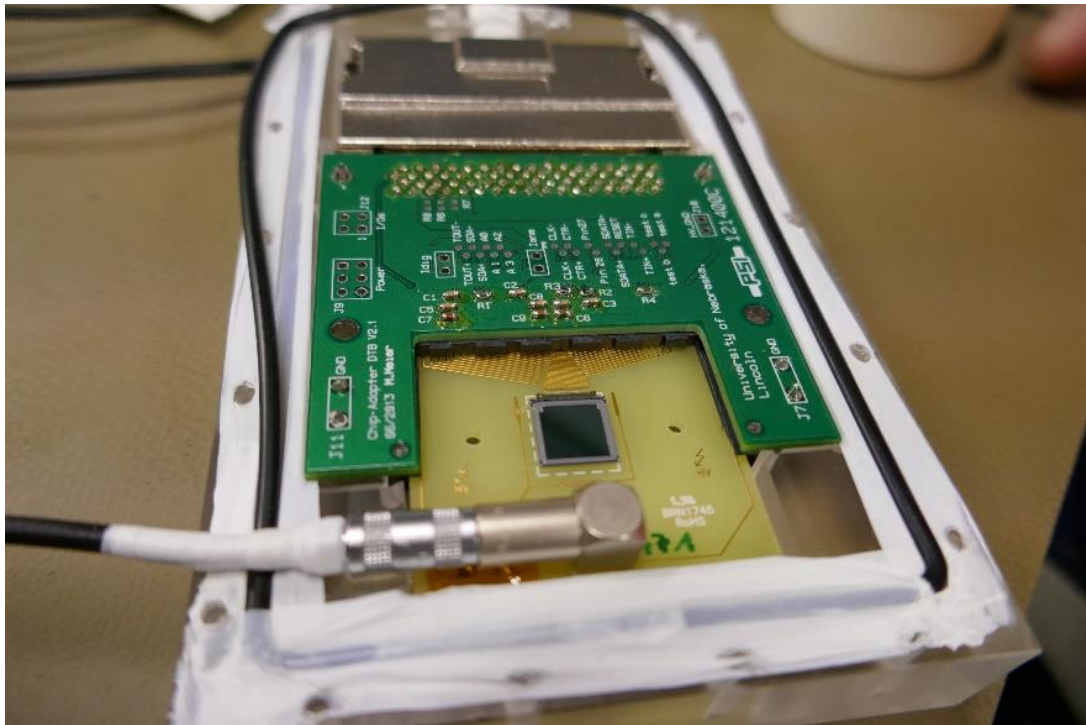


Figure 42. The lower half of a transparent box with a detector and adapter card, cables inserted. The top of the box is screwed to the lower half

The water phantom (shown in Figure 43 as well as the rest setup parts) was positioned on a table at a distance of 95 cm from the  $^{60}\text{Co}$  gamma ray source, the picture of the source is in Figure 44. A typical activity of different isotopes used for diagnostic applications including brain, lung, liver, kidney, and bone scanning is varying from 0.1 to 50 mCi, where 1 mCi = 3.7 Bq [38]. The activity of the source was 449 TBq on 01.05.2010.

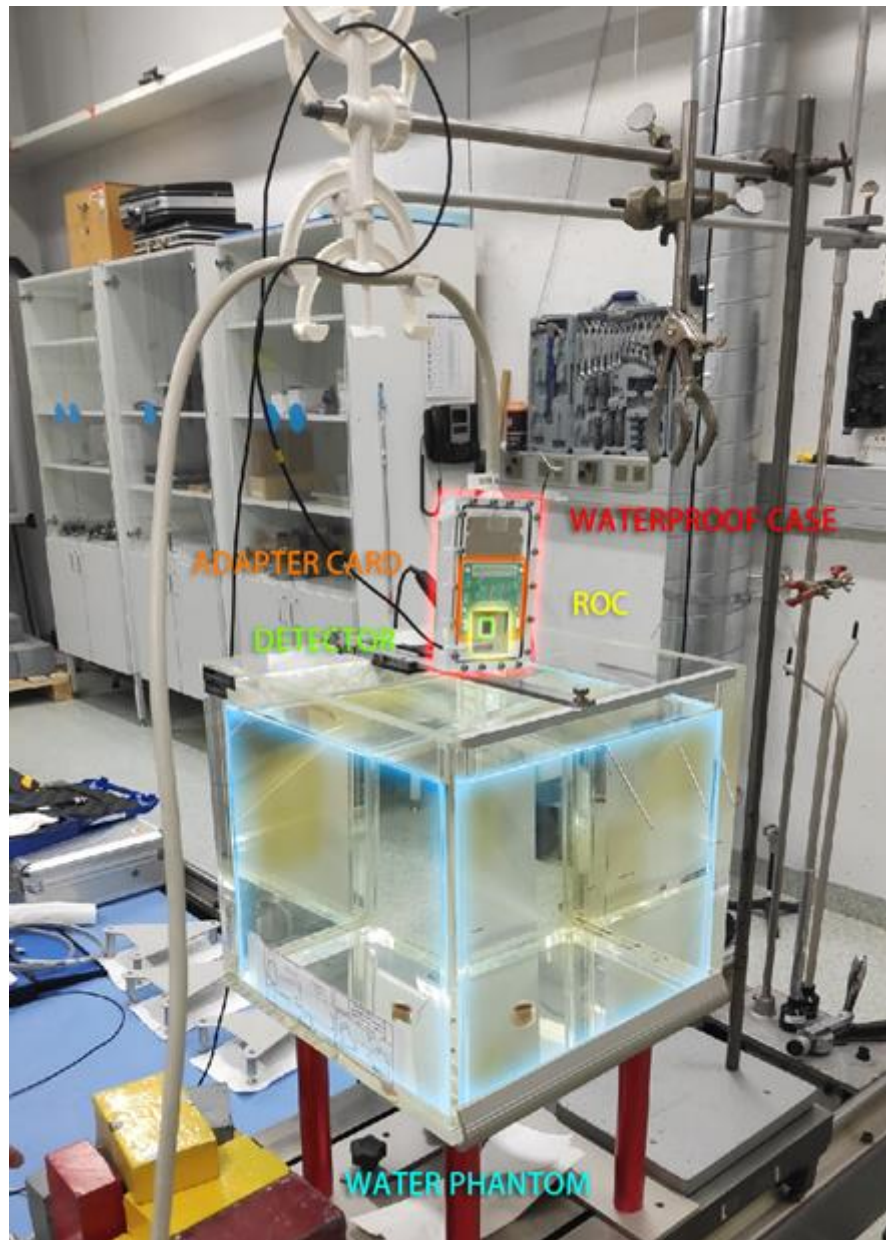


Figure 43. The setup used for the  $^{60}\text{Co}$  test runs. The main parts are highlighted



Figure 44.  $^{60}\text{Co}$  gamma ray source Gammabeam X200, manufactured by Best Theratronics (Ottawa, Canada)

The underwater test with a strong gamma ray source is the closest simulation of the real usage of the CMS 47A silicon pixel detector for medical visualization purposes that could be achieved during the measuring campaign.

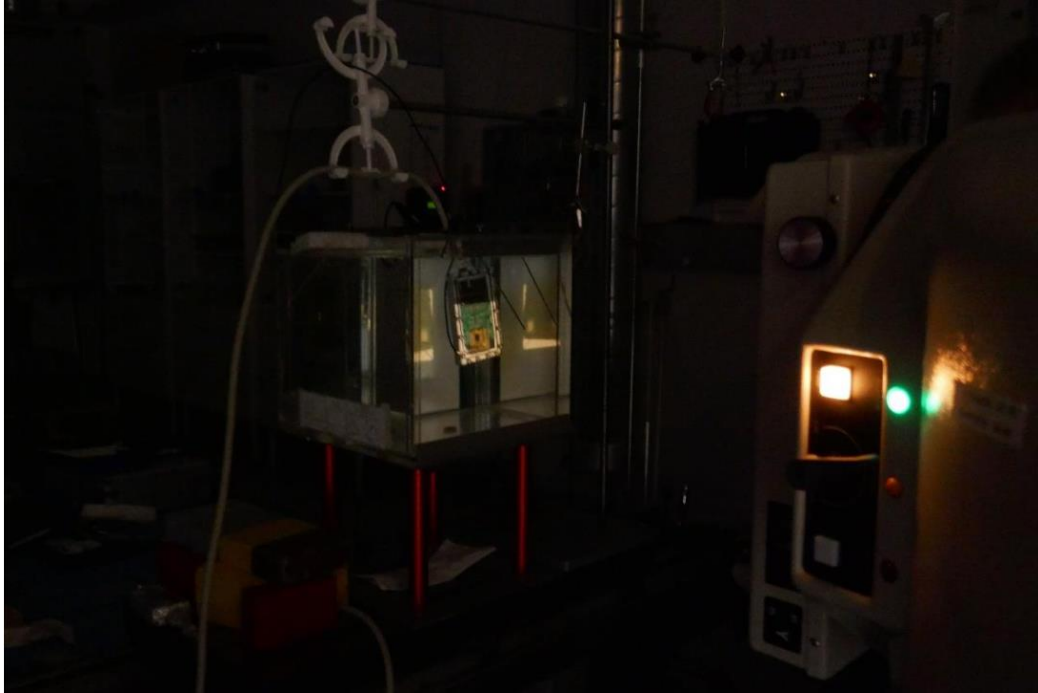


Figure 45. Transparent box with detector inside the water tank, alignment performed with lights. The  $^{60}\text{Co}$  source and a collimator visible on the right edge of the image

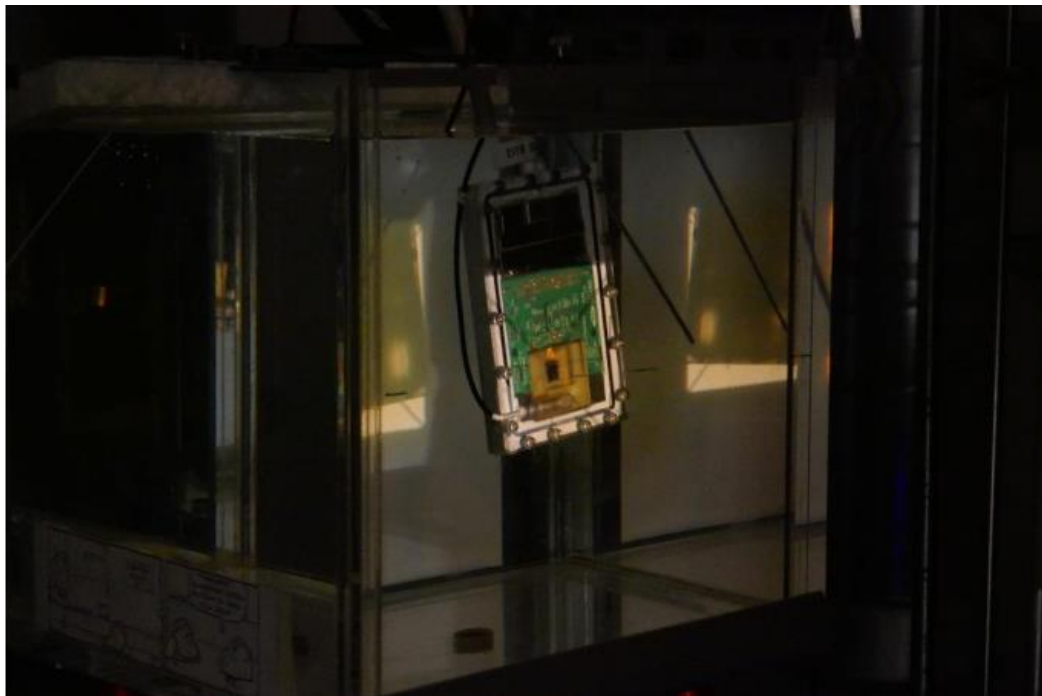


Figure 46. Transparent box with the detector inside the water tank at the center position, aligned with lights

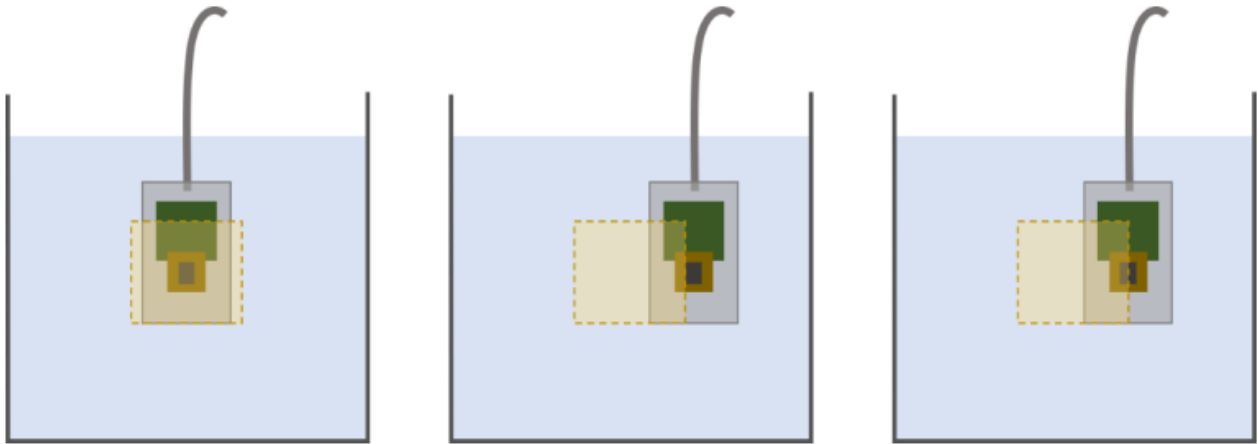


Figure 47. A sketch of the transparent box positions with the detector in the water tank.

The position of the gamma ray beam is marked as a yellow dashed line. From left to right: “center” (not marked explicitly in the journal), “edge”, “halfway”. Measurement series was done with box towards the front of the tank

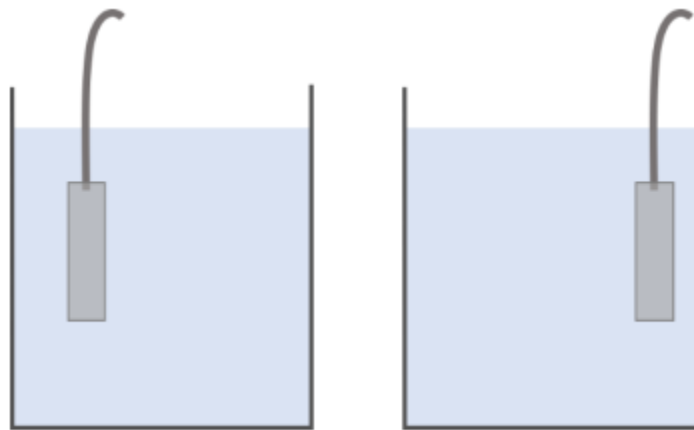


Figure 48. Sketch of the transparent box positions with the detector in the water tank seen from the side. Left is marked as “center” (not marked explicitly in the journal), right is marked as “back”. Measurement at the back of the tank was done in the “center” position

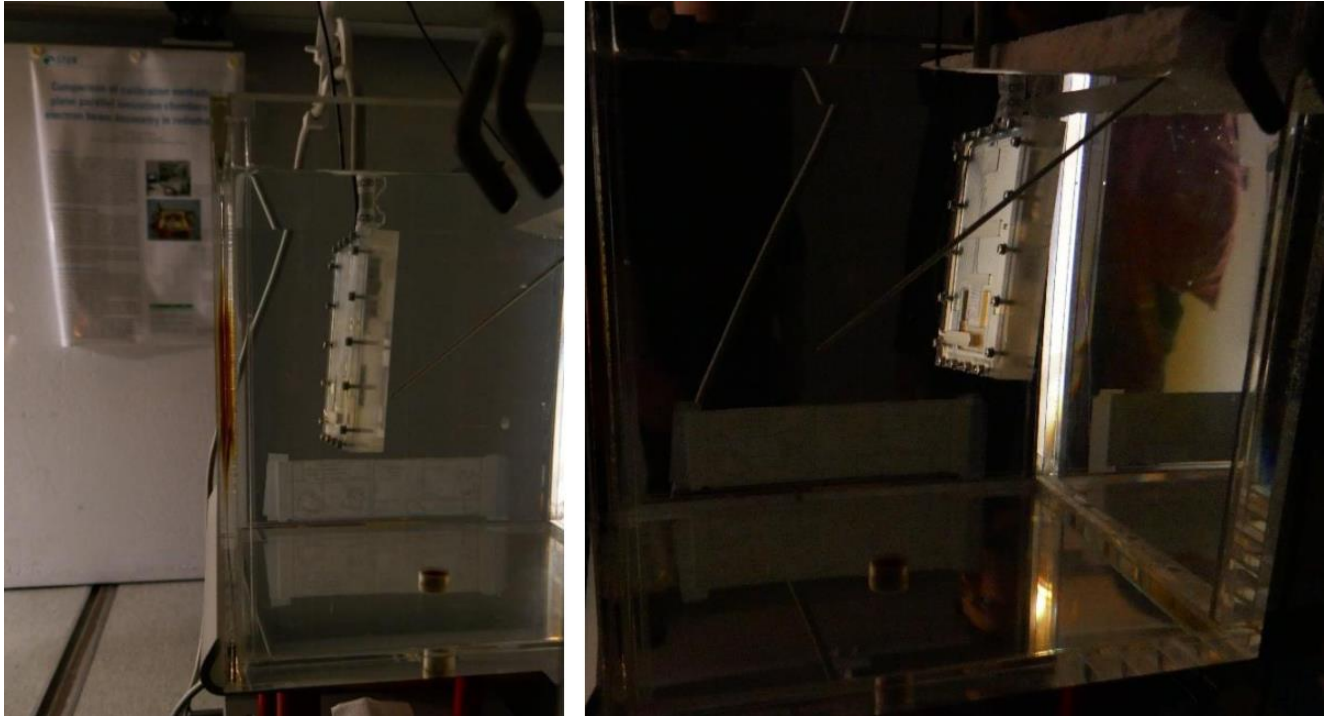


Figure 49. Photographs of the transparent box positions with the detector in the water tank seen from the side. Left is “center” (not marked explicitly in files), right is “back”

The hitmaps shown in Figures 50 - 53 are correlating with the detector position in the water phantom. For the “edge” (Figure 52) and the “halfway” (Figure 53) positions the gradient in the number of entries is observed. The “back” position hitmap has a much smaller number of entries than the “center” one. This is due to the fact that the ionizing radiation has to penetrate a thicker water volume and hence lose more energy. Registered events are thus originating from the secondary ionization, not the gamma rays. The spectra obtained during the underwater tests are shown in Figure 54.

The numbers of entries for the broad X-rays and the  $^{60}\text{Co}$  gamma beam source are: 2,732,995 entries for the strongest used RQR-6 (41.64 keV) X-ray tube radiation, 3,771,721 entries for the “center” detector position, and 1,430,087 entries for the “back” detector position. Entries include all negative effects like charge sharing and pile-up.

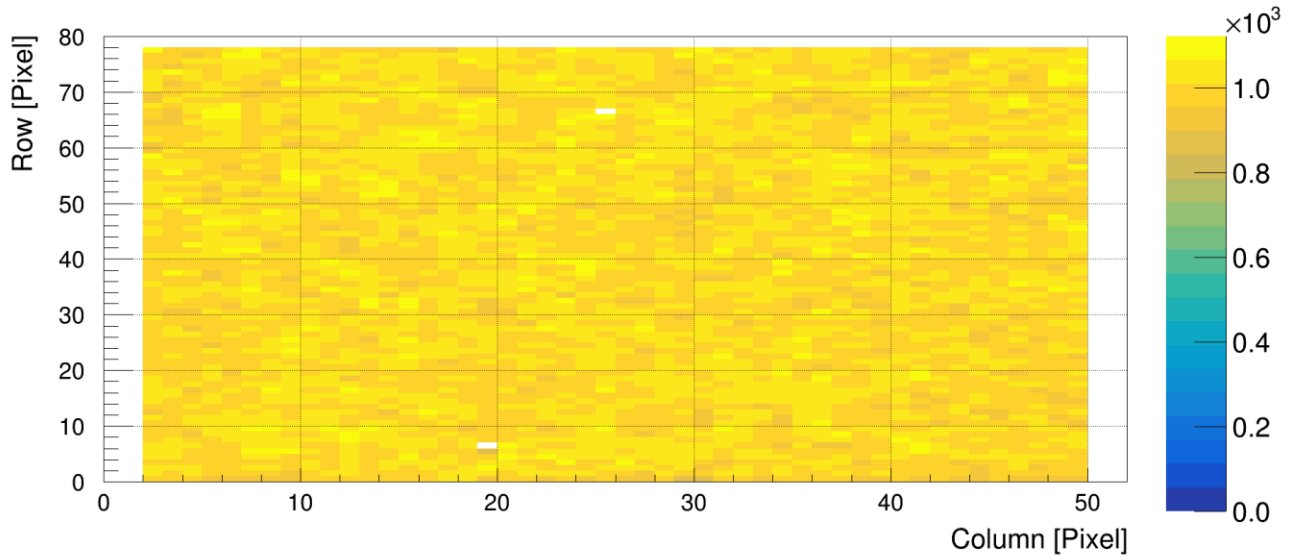


Figure 50. Hitmap of the CMS 47A in the “center” position. This hitmap represents the position with the most registered events

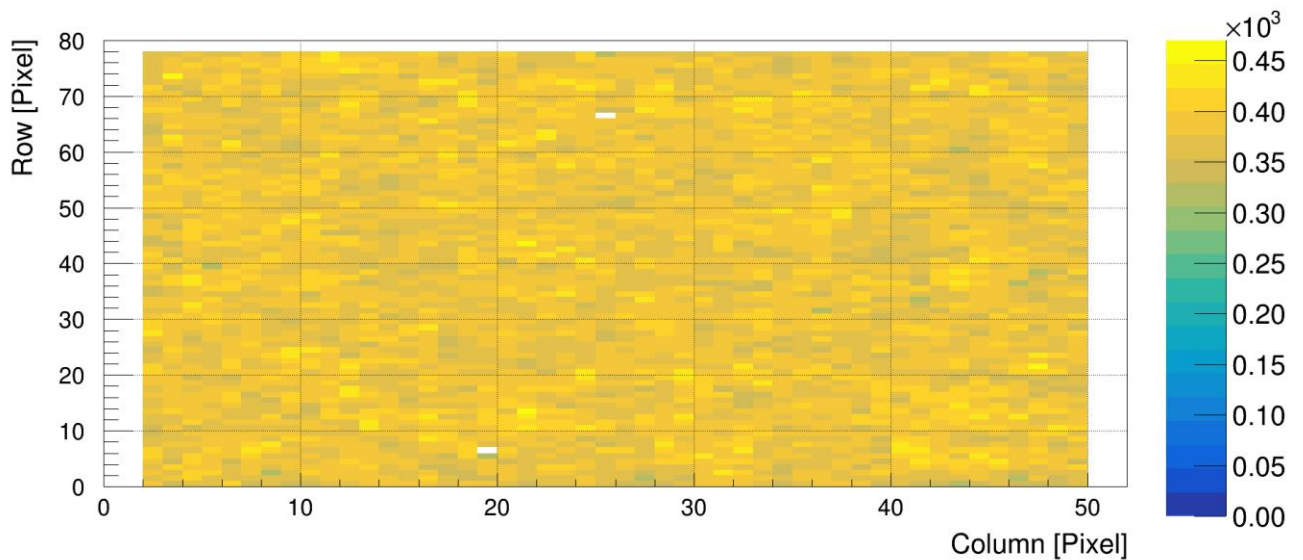


Figure 51. Hitmap of the CMS 47A in the “back” position. This hitmap represents the position of the detector being placed behind the thick water volume that represents the human body

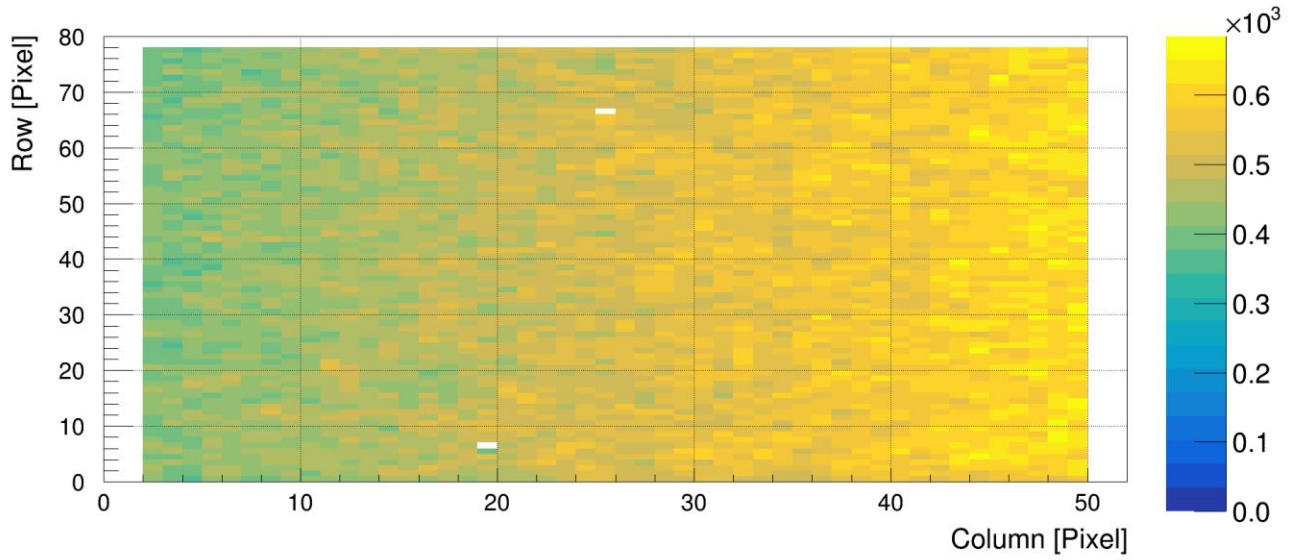


Figure 52. Hitmap of the CMS 47A in the “edge” position. The gradient in the number of registered events related to the position of the detector can be observed

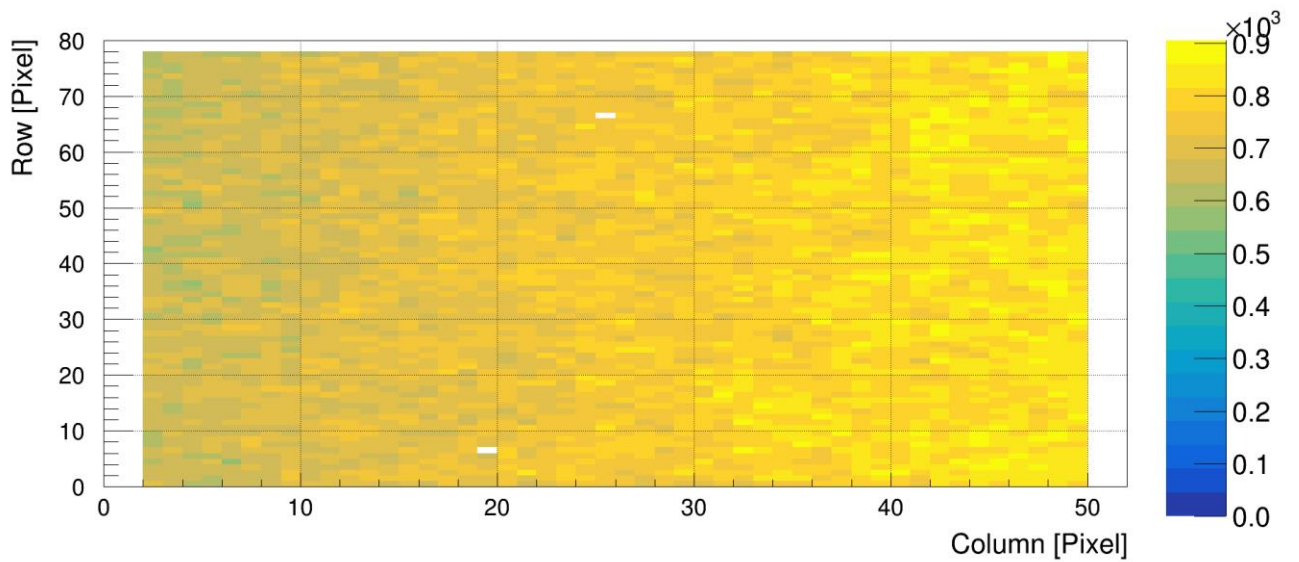


Figure 53. Hitmap of the CMS 47A in the “halfway” position. The gradient in the number of registered events on the left side can be seen

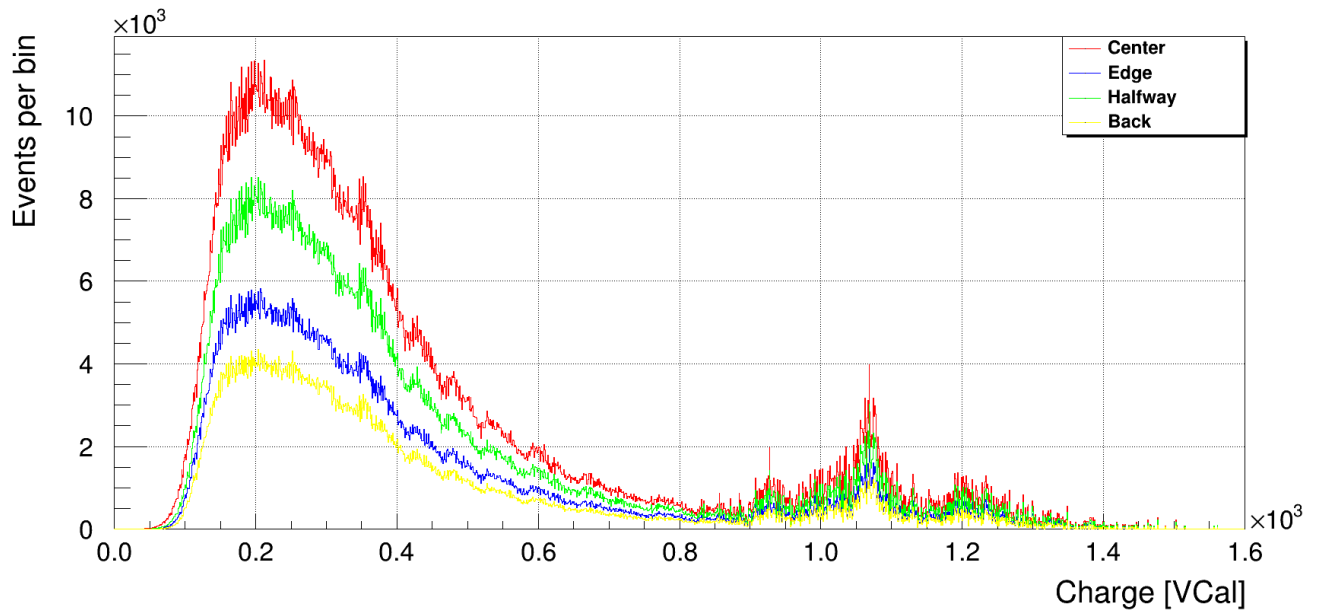


Figure 54. The spectra obtained during the underwater tests with the  $^{60}\text{Co}$  source

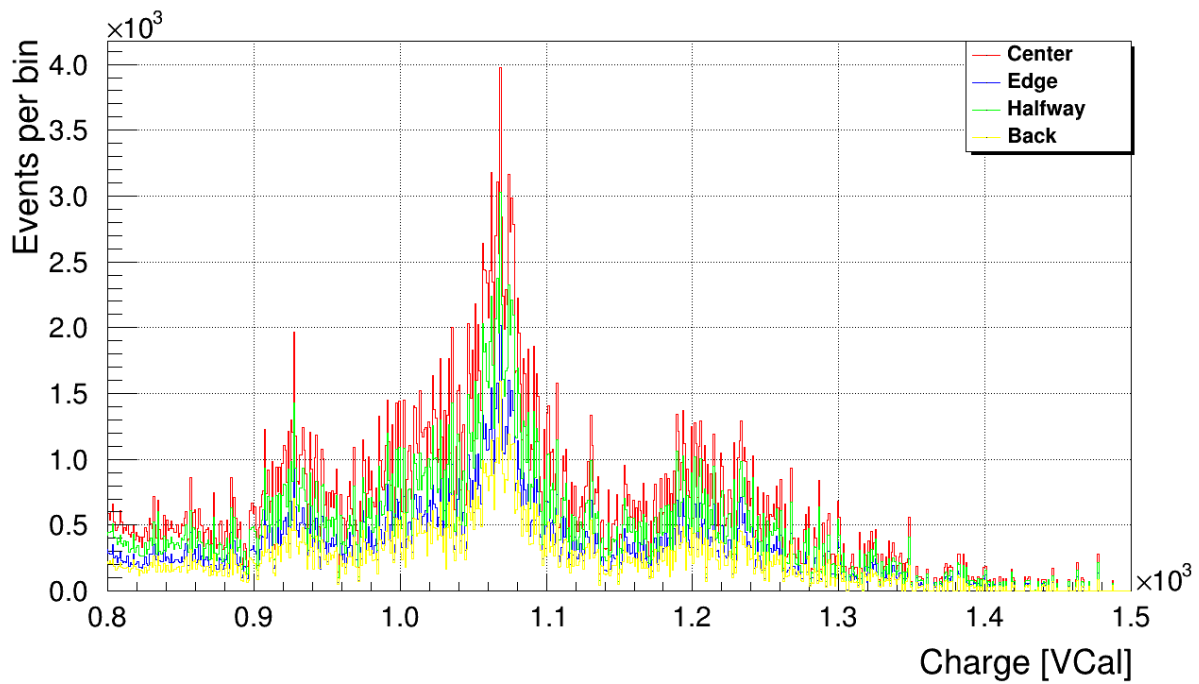


Figure 55. Closer picture of “peaks” that are due to the ROC limitations

#### 4. ANALYSIS OF RESULTS

With the X-ray box test, the detector module functionality was checked before the testing campaign at STUK, which is a time saver. However, the X-ray box tests give much less information and much harder to analyze compared with the measurements with STUK X-rays. The results for the AM-241 tests with the AC-coupled A1 silicon detector can provide more information regarding the ROC and DAQ software working principles.

X-Ray tube measurements performed in STUK provided some interesting data to analyze. The important observation is that there was no peak shift observed with the increase in current for the same radiation quality for narrow and broad X-rays. Tests with broad X-Rays provided some odd results like low energy noise which does not correspond to the fluence spectra or the shift of the spectrum endpoint when the fluence is increased. The reason is most likely is in the detector response, scattering, and pile-up, but yet to be confirmed.

Typical  $^{60}\text{Co}$  radiation source releases one electron with 317.9 keV energy and two gamma rays during the nucleon decay, the spectrum, therefore, has two strong gamma peaks at the energies of 1.173 MeV and 1.332 MeV. The peaks of the obtained spectra at 1.067 VCal and 1.208 VCal (shown in Figure 55) are not the  $^{60}\text{Co}$  peaks. The  $^{60}\text{Co}$  gamma beam cannot be detected directly, unlike the events originating from the secondary ionization. The readout chip is limited to around 300 keV by the preamplifier and the ADC, therefore, some of  $^{60}\text{Co}$  electrons can be detected and form the resulting spectra. Since the ROC has a limitation of 300 keV, the peaks might be the secondary ionization products from the scattering of the  $^{60}\text{Co}$  radiation. In addition, electrons scattered from  $^{60}\text{Co}$  photons have energies about a few hundred keV and can bring the impact to the resulting spectra.

The inability to detect the gamma radiation is not critical, as the main application of this test is beam dose profiling rather than characterization of specific X-ray energy.

## 5. CONCLUSIONS

The tests presented in this work were completed successfully and provided some valuable improvements compared to the previous tests at STUK. The general ESD safety was improved by using ESD bracelets every time the PCB with the ROC was handled. The data from this measuring campaign also provided a much better understanding of the pXar DAQ software and especially of the trimming functionality of the ROC.

The limitations of used PSI46dig ROC have to be addressed, including the limitation to a maximum energy of 300 keV by the preamplifier and ADC. Thus, there was no direct detection of the  $^{60}\text{Co}$  gamma rays. The silicon bulk layer of CMS 47A is very thin (280  $\mu\text{m}$ ), which makes the detection even more difficult.

With the collected data it might be possible to obtain event-by-event information and separate events with pixel localization using clustering, which was not implemented before. The algorithm for the clusterization of charge deposition is yet to be introduced. Event-by-event information can be a key to increase the applicability of the CMS 47A pixel detector for medical visualization or at least give more information on how to improve the performance of the detector and the PSI46dig ROC.

Some improvements for future testing can be made:

- It is important to verify trimming settings and noisy pixels with a noise run whenever the energy/beam current of the tube or the position of the detector is changed. The change in location can cause changes in noise, so additional pixels have to be masked.
- The plastic box used for the X-ray tube tests was positioned so that the bottom side (the PCB and ROC) were facing the sources. A new box has to be made to reduce the scattering in the plastic and PCB before the radiation reaches the active volume of the detector. A thin window of a light material like aluminum or Kapton should be made on top of the detector casing for the same reasons.

- Emptying the buffer of the DTB takes very long especially when recording event-by-event runs. This has been pinpointed to the FPGA of the DTB which cannot handle certain actions simultaneously. It is a far smaller problem when the intensities of X-rays are high, as it was in STUK because the number of empty events is very low and even short runs can provide good enough information.

Designed normalization script was successfully implemented to convert VCal units to keV, which are much easier to understand and work with. This script will be used for the data analysis of the results that will be obtained during the future measuring campaigns.

## SUMMARY

The development of a modern precise detector for medical visualization purposes is a tough challenge. One of the possible ways to create such a device is to employ a direct detection system based on photon counting with silicon pixel sensors, using readout electronics developed for high-energy physics experiments.

During this thesis work silicon pixel detectors, including the single-chip variation of pixel module of the phase 1 CMS pixel tracker named CMS 47A, were tested under various radiation average energies (including different radiation sources), tube currents, and voltages. The energy spectra and hitmaps were obtained. The unique experiment with the detector inside a water phantom that simulates the human body was carried out and provided a lot of information on the detector functionality under the strong  $^{60}\text{Co}$  gamma ray source.

The unique experimental data provided a much better understanding of the pXar DAQ software and especially of the trimming functionality of the ROC. The limitations of used PSI46dig ROC have to be addressed. The event-by-event information can be a key to increase the applicability of the CMS pixel detector for medical visualization once the clusterization algorithm is implemented. Designed normalization script was successfully used to convert VCal units to keV, which are much easier to understand and work with. The list of improvements for future tests was formed.

## REFERENCES

- [1] Evans, L. LHC Machine [Text] / L. Evans, [et all.] // Journal of Instrumentation. 2008. V. 3. P. 164.
- [2] Aad, G. The ATLAS Experiment at the CERN Large Hadron Collider [Text] / G. Aad, [et all.] // Journal of Instrumentation. 2008. V. 3. P. 437.
- [3] Adolphi, R. The CMS experiment at the CERN Large Hadron Collider [Text] / R. Adolphi, [et all.] // Journal of Instrumentation. 2008. V. 3. P. 361.
- [4] Aamodt, K. The ALICE experiment at the CERN Large Hadron Collider [Text] / K. Aamodt, [et all.] // Journal of Instrumentation. 2008. V. 3. P. 259.
- [5] Alves, A. The LHCb Detector at the CERN Large Hadron Collider, [Text] / A. Alves, [et all.] // Journal of Instrumentation. 2008. V. 3. P. 217.
- [6] Acosta, D. CMS Physics Detector Performance and Software, [Text] / D. Acosta, [et all.] // Technical Design Report 2006. V. 1. P. 521.
- [7] CMS Phase II Upgrade Scope Document. Access: <http://cds.cern.ch/record/2055167/files/LHCC-G-165.pdf?subformat=pdfa&version=4>.
- [8] Alagöz, E. Simulation and beam test measurements of the CMS pixel detector Access: [http://unizh.web.cern.ch/Publications/Articles/Alagoz\\_thesis.pdf](http://unizh.web.cern.ch/Publications/Articles/Alagoz_thesis.pdf).
- [9] CMS tracker technical design report Access: <https://s3.cern.ch/inspire-prod-files-0/05a1ef8b82c462ee8950c22f45c5a099>.
- [10] Hartmann, F. Evolution of Silicon Sensor Technology in Particle Physics [Text] / F. Hartmann. Cham, Switzerland: Springer International Publishing AG, 2017. P. 386.
- [11] Akgun, B. Performance of the CMS Phase 1 Pixel Detector [Text] / B. Akgun, [et all.] // Journal of Instrumentation. 2016. V. 11. P. 9.
- [12] Dominguez, CMS Technical Design Report for the Pixel Detector Upgrade [Text] / A. Dominguez, [et all.] // Technical Design Report. 2012. V. 11. P. 264.

[13] The CMS Collaboration Technical Proposal for the Upgrade of the CMS Detector through 2020. Access: <https://cds.cern.ch/record/1355706/files/LHCC-P-004.pdf>.

[14] Allport, P. Applications of Silicon Strip and Pixel-based Particle Tracking Detectors, [Text] / P. Allport, [et all.] // Nat Rec Phys. V. 1. 2019. P. 567-576.

[15] Barbiellini, G. Solid-state detectors for X-rays from synchrotron radiation [Text] / L. Andreucci, [et all.] // World Scientific V. 2. 1992. P. 608.

[16] Beuville, E. High Resolution X-ray Imaging Using a Silicon Strip Detector [Text] / E. Beuville, [et all.] // IEEE Transactions on Nuclear Science. V. 45. 1998. P. 3059-3063.

[17] Atomic and Molerucal data NIST . Access: <http://www.nist.gov/pml/data/>.

[18] Sadrozinski, H. Particle detector applications in medicine [Text] / H. Sadrozinski, [et all.] // Nuclear Instruments and Methods in Physics. – V. 732. 2013. P. 34-39.

[19] PhysicsOpenLab. Access: <http://physicsopenlab.org/2017/08/02/bremsstrahlung-radiation>.

[20] Knop, G. Interaction of Electrons and Alpha Particles with Matter [Text] / G. Knop, [et all.] // Alpha- Beta- and Gamma Ray Spectroscopy. V. 1. – 1968. P. 36.

[21] Bohr, N. Mat. Fys. Medd. [Text] / N. Bohr, [et all.] // Kgl. Dan. Vid. Selsk. V. 18. 1948. P. 418.

[22] Bethe, H. Passage of Radiation though Matter [Text] / H. Bethe, [et all.] // Experimental Nuclear Physics. V. 1. 1953. P. 166.

[23] Sadauskis, J. Methods in Experimental Physics [Text] / J. Sadauskis, [et all.] // Phys. Rev. V. 4. 1967. P. 319-491.

[24] Nelson, G. Gamma-Ray Interactions with Matter [Text] / G. Nelson, [et all.] // Passive Nondestructive Analysis of Nuclear Materials. V. 2. 1991. – P. 27-42.

[25] Gill, K. Bulk Damage Effects in Irradiated Silicon Detectors due to Clustered Divacancies [Text] / K. Gill, [et all.] // Journal of Applied Physics V. 86. 1997. P. 126.

[26] Summers, G. Displacement Damage Analogs to Ionizing Radiation Effects [Text] / G. Summers, [et all.] // Radiation Measurements. V. 24. 1995. P. 1-8.

[27] Oen, O. Bulk Processing of Materials with Radiation [Text] / O. Oen, [et all.] // Journal of Applied Physics V. 30. 1959. P. 1289-1295.

[28] Summers, G. Damage Correlations in Semiconductors Exposed to Gamma [Text] / G. Summers, [et all.] // IEEE Transactions on Nuclear Science V. 40. 1993. P. 1221-1226.

[29] Cahn, J. Measurement of Thermal Conductivity by Utilization of the Peltier Effect [Text] / J. Cahn, [et all.] // Journal of Applied Physics V. 30. 1959. – P. 1351.

[30] Moll, M. Radiation Damage in Silicon Particle Detectors: Microscopic Defects and Macroscopic Properties [Text] / M. Moll, [et all.] // Ph.D. thesis, Hamburg University 1999.– P. 251.

[31] Lemeilleur, F. Third RD48 status report: the ROSE collaboration Third [Text] / F. Lemeilleur, [et all.] // Status Report. 2000. V. 3. P. 42.

[32] Harkonen, J. RD50 Status Report [Text] / J. Harkonen, [et all.] // Technical Report 2005. P. 113.

[33] Zhen-An, L. Proceedings of International Conference on Technology and Instrumentation in Particle Physics [Text] / L. Zhen-An, [et all.] // Springer International Publishing AG 2018. V. 2. P. 437.

[34] Gray, J. The CMS Phase-1 Pixel Detector [Text] / J. Gray, [et all.] // 13th Topical Seminar on Innovative Particle and Radiation Detectors, Journal of Instrumentation 2016. V. 1. P. 4.

[35] PIXEL DTB Testboard for Readout Chips Manual. Access: <https://twiki.cern.ch/twiki/bin/viewauth/CMS/PixelDTB>.

[36] Antonelli, J. FPix Module Testing Reference Guide, [Text] / J. Antonelli, [et all.] // Journal of Instrumentation 2019. V. 1. P. 15.

[37] Tikkanen, J. Muunnoskertoimien ilmakermasta annosekvivalenttiin laskeminen ISO N- ja ISO H -röntgensäteilylaaduille spektristä sekä Ortec'in GEM-S5020P -spektrometrin mallintaminen [Text] / J. Tikkanen, [et all.] // STUK-TR 30 Experimental Report 2019. P. 34.

[38] Medical Imaging and Diagnostics. Access: <https://courses.lumenlearning.com/physics/chapter/32-1-medical-imaging-and-diagnostics/>.

[39] Vernieri, C. The CMS Pixel detector from Physics to Technology [Slides] / C. Vernieri // Fermilab 2016. P. 55.

[40] Ott, J. HIP Pixel 2018 Layout and Naming Conventions [Slides] / J. Ott // HIP 2018. P. 22.

[41] Ott, J. Processing of AC-coupled n-in-p Pixel Detectors on MCz Silicon using Atomic Layer Deposited Aluminium Oxide [Text] / J. Ott, [et all.] // Nuclear Instruments and Methods in Physics Research 2019. P. 6.

## APPENDICES

### Appendix A. Test journal

Table A1. Irradiation run with CMS Si pixel detector

Measurement number	Radiation quality	Tube current (mA)	Run duration (sec)	Commentary
Using 160 kV x-ray tube				
1	ISON-30	1	100	
2	ISON-30	5	100	
3	ISON-30	10	100	
4	ISON-30	20	100	
4.1 (filltree)	ISON-30	20	400	
5	ISON-30	40	100	
6	ISON-40	20	100	
7	ISON-40(with filter)	20	100	2 <sup>nd</sup> peak is observed better with filter
8	ISON-60	20	100	Peaks are separated, 1 <sup>st</sup> one is probably scattered radiation
8.1	ISON-60	20	300	Peaks are defined; leakage current 0.128 uA
X-ray tube was changed from 160 kV to 320 kV				
9	ISON-80	20	100	High noise
10	ISON-80	30	100	High noise
11	ISON-80	40	100	
12	ISON-100	20	200	The picture is bad,

				Noise is shifted to the right (110 Vcal)
Using broad X-rays				
13	RQR-2	20	200	The peak is broader, Al filter is thinner
14	RQR-2	10	200	Fewer events with 10 mA, 20 mA is optimal
15	RQR-4	20	100	
16	RQR-6	20	100	Tail increased; peak did not move
17 (filltree)	RQR-6	20	100	
18 (filltree)	RQR-6	20	100	

Table A2. Irradiation run with AC-coupled Si pixel detector G1

Measurement number	Radiation quality	Tube current (mA)	Run duration (sec)	Commentary
Using 160 kV x-ray tube				
1	ISON-30	20	100	
2	ISON-40	20	100	
3	ISON-60	20	100	Peaks shifted according to the voltage; leakage current 0.2 uA
Tests with Am241. Tests 1 - 5 had no good results, test 6 with visible peaks				
4	ISON-80	20	100	
5 (filltree)	ISON-80	20	150	

Table A3. Underwater irradiation run with CMS single-chip Si pixel detector

Measurement number	Location in the water tank	Leakage current (uA)	Run duration (sec)	Commentary
1	Center, front	0.273	60	
2 (filltree)	Center, front	0.290	60	
3	Edge, front	0.223	60	
4 (filltree)	Edge, front	0.230	60	
5	Edge, front	0.210	60	With metal stripe on the tank wall in front of the detector
6	Halfway, front	0.250	60	
7 (filltree)	Halfway front	0.236	60	
8 (filltree)	Center, back	0.175	60	

## Appendix B. X-ray characteristics

Table B1. Narrow X-rays characteristics

ISO Narrow -säteilylaadut				2 m distance							
Radiation quality	Average energy	X-ray tube	Control panel reading	Tube current	Air kerma rate		Monitor chamber reading	Additional filtration			
	[keV]	[kV]	[kV]	[mA]	[mGy/h]	[ $\mu$ Gy/s]	[nA]	Al	Cu	Sn	Pb
ISO N-10 <sup>2</sup>	8	160	8.5					0,1	-		
ISO N-15 <sup>2</sup>	12	160	12.6	20.0	26.76	7.433	0.1995	0,5	-		
ISO N-20	16	160	17.8	30.0	87.74	24.372	0.3916	1,0	-		
ISO N-25	20	160	23.7	30.0	98.79	27.442	0.3615	2,0	-		
ISO N-30	24	160	28.4	31.0	56.06	15.571	0.1995	4,0	-		
ISO N-40	33	160	38.5	33.0	26.01	7.226	0.1036	4,0	0,21		
ISO N-60	48	160	59	38.0	55.23	15.341	0.2460	4,0	0,6		
ISO N-80	65	320	78	29.0	20.13	5.593	0.0828	3,9	2,0	-	-
ISO N-100	83	320	98	29.0	9.88	2.745	0.0402	3,9	5,0	-	-
ISO N-120	100	320	118	24.0	9.15	2.540	0.0384	3,9	5,0	1,0	-
ISO N-150	118	320	148	4.8	14.08	3.911	0.0605	3,9	-	2,5	-
ISO N-200	164	320	198	14.0	15.66	4.351	0.0850	3,9	2,0	3,0	1,0
ISO N-250	208	320	248	11.0	12.86	3.572	0.0768	3,9	-	2,0	3,0
ISO N-300	250	320	298	9.0	10.84	3.011	0.0701	3,9	-	3,0	5,0

Table B2. Broad X-rays characteristics

Radiation quality	Mean Energy	Voltage	Tube current	Additional filtration
	[keV]	[kV]	[mA]	[mmAl]
RQR 2	27.03	40	32,2	2,59
RQR 3	30.78	50	16,9	2,59
RQR 4	34.44	60	12,1	2,78
RQR 5	38.2	70	9,2	2,86
RQR 6	41.64	80	7,3	3,02
RQR 7	44.6	90	6,2	3,25
RQR 8	48.64	100	5,2	3,37
RQR 9	56.2	120	4,0	3,82